

Critical behavior of the dimerized Si(001) surface: A continuous order-disorder phase transition in the 2D Ising universality class

Christian Brand,^{1,*} Alfred Hucht,^{1,2} Hamid Mehdipour,¹ Giriraj Jnawali,^{1,†}
 Jonas D. Fortmann,¹ Mohammad Tajik,¹ Rüdiger Hild,¹ Björn Sothmann,^{1,2}
 Peter Kratzer,^{1,2} Ralf Schützhold,^{3,4} and Michael Horn-von Hoegen^{1,2}

¹*Faculty of Physics, University of Duisburg-Essen, 47057 Duisburg, Germany*

²*Center for Nanointegration (CENIDE),
 University of Duisburg-Essen, 47057 Duisburg, Germany*

³*Institute of Theoretical Physics, Dresden
 University of Technology, 01062 Dresden, Germany*

⁴*Helmholtz-Zentrum Dresden-Rossendorf, 01328 Dresden, Germany*

(Dated: October 25, 2023)

Abstract

The critical behavior of the order-disorder phase transition in the buckled dimer structure of the Si(001) surface is investigated both theoretically by means of first-principles calculations and experimentally by spot profile analysis low-energy electron diffraction (SPA-LEED). We use density functional theory (DFT) with three different functionals commonly used for Si to determine the coupling constants of an effective lattice Hamiltonian describing the dimer interactions. Experimentally, the phase transition from the low-temperature $c(4\times 2)$ - to the high-temperature $p(2\times 1)$ -reconstructed surface is followed through the intensity and width of the superstructure spots within the temperature range of 78-400 K. Near the critical temperature $T_c = 190.6$ K, we observe universal critical behavior of spot intensities and correlation lengths which falls into the universality class of the two-dimensional (2D) Ising model. From the ratio of correlation lengths along and across the dimer rows we determine effective nearest-neighbor couplings of an anisotropic 2D Ising model, $J_{\parallel} = (-24.9 \pm 0.9_{\text{stat}} \pm 1.3_{\text{sys}})$ meV and $J_{\perp} = (-0.8 \pm 0.1_{\text{stat}})$ meV. We find that the experimentally determined coupling constants of the Ising model can be reconciled with those of the more complex lattice Hamiltonian from DFT when the critical behavior is of primary interest. The anisotropy of the interactions derived from the experimental data via the 2D Ising model is best matched by DFT calculations using the PBEsol functional. The trends in the calculated anisotropy are consistent with the surface stress anisotropy predicted by the DFT functionals, pointing towards the role of surface stress reduction as a driving force for establishing the $c(4\times 2)$ -reconstructed ground state.

I. INTRODUCTION

Materials with reduced dimensions often exhibit energetically close-lying metastable states due to combined instabilities of the electron and the lattice system. Examples in one-dimension (1D) include the formation of charge density waves, doubling of periodicity driven by a Peierls distortion, or symmetry breaking through a Jahn-Teller instability [1–4]. In purely 1D structures, these instabilities are predicted to exist only for $T = 0$ K. Even smallest thermal excitations drive the system into the high temperature state. Only those interactions mediated by higher dimensions, e.g., the coupling of parallel 1D atomic wires

* Corresponding author: christian.brand@uni-due.de

† Current address: Department of Physics, University of Cincinnati, Cincinnati, OH 45221, USA

perpendicular to the wire direction, stabilize the instability at finite temperatures. Examples for such systems are adsorbate-induced atomic wires such as Si(553)-Au [5–8], Si(557)-Pb [9–12], Ge(110)-Pt [13] and Si(111)-In [14, 15].

A truly famous example of such a 1D structure with weak coupling in the second dimension is the bare Si(001) surface exhibiting a so-called dimer reconstruction [16–18]. The bulk-terminated Si surface exhibits two half-filled dangling bonds per atom which makes the Si(001) surface electronically unstable. Since thermodynamics always tend to minimize the surface free energy, these dangling bonds form dimers, leading to a doubling of the periodicity doubling along the dimer axis and thus forming a reconstruction on the Si(001) surface [19–21]. These dimers, which are alternately buckled at low temperatures [22], are arranged in parallel rows. At low temperatures, the adjacent dimer rows are arranged in an anti-phase registry, leading to a $c(4\times 2)$ reconstruction as the ordered ground state [23, 24]. The buckling orientation can be formally assigned to an up- or down-spin, i.e., a two-dimensional (2D) antiferromagnetic order arises. This system is known for the experimental observation of a continuous order-disorder phase transition that occurs at $T_c \approx 200$ K from the $c(4\times 2)$ to the $p(2\times 1)$ high temperature state [25]. Similar to silicon, the Ge(001) surface also exhibits such a structural phase transition from a $c(4\times 2)$ to a $p(2\times 1)$ reconstruction at slightly higher temperature [26–30]. Kevan *et al.* [31] suggested that this order-disorder phase transition occurs via a two-step process for Ge(001). Details of the phase transition on Ge(001) can be found elsewhere [26].

Although the order-disorder phase transition for the dimerized Si(001) surface has been known for decades, the critical behavior has yet not been studied in detail. Previous studies were constrained by the limited instrumental resolution of low energy electron diffraction (LEED) and the pinning of the phase transition by the extreme sensitivity of the surface to adsorbates or the omnipresent atomic steps that prevent large-scale spatial fluctuations [25, 32–34]. Also, experimental findings such as the observation of streaklike diffuse intensity [32] could not be explained by the theory [35].

Very recently, we showed that the Si(001) order-disorder phase transition can be described by an anisotropic 2D Ising model with $T_c = 190.6$ K [36]. The critical behavior of the order parameter, the fluctuations and the correlation lengths were analyzed in the framework of the 2D Ising universality class [37, 38] and were mapped onto the exactly solved nearest-neighbor 2D Ising model [39, 40]. The experimentally determined coupling energies $J_{\parallel} = -24.9$ meV

and $J_{\perp} = -0.8 \text{ meV}$ along and across the dimer rows, respectively, were in agreement with some previously conducted *ab initio* density functional theory (DFT) calculations, while other such calculations deviated from the experimental results. To elucidate of the microscopic interactions involved, we performed comprehensive DFT calculations with three different exchange-correlation functionals. Our work thus helps to resolve the long-standing debate as to why some theoretical predictions of T_c (e.g. $T_c = 316 \text{ K}$ [35]) differ from the experimental value.

This paper is organized as follows: After summarizing the current understanding of the energetic hierarchy of the Si(001) surface structure in Sec. II, we review the techniques for setting up lattice Hamiltonians for the Si(001) surface and present our interaction parameters calculated from DFT in Sec. III. We then argue that, as far as the critical behavior close to the order-disorder transition is concerned, the lattice Hamiltonian can be reduced to an anisotropic 2D Ising Hamiltonian with two effective parameters (Sec. IV). The analytically known scaling laws of the 2D Ising model allow us to precisely determine T_c and the ratio of the interaction parameters. In Section V the experimental data analysis used in Ref. 36 is explained in more detail. Finally, we conclude and give an outlook on possible future work. In the Appendix we compare the results of our DFT calculations with previous work.

II. DIMERIZED SI(001) SURFACE

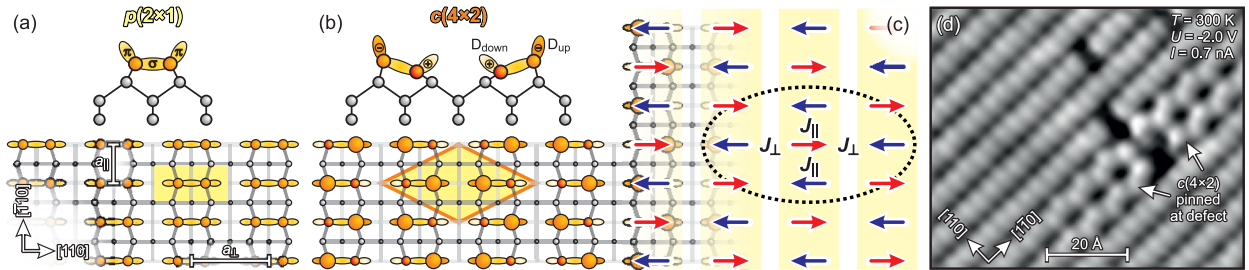


FIG. 1. **Dimer reconstruction of Si(001).** Atomic structure models of the Si(001) surface for (a) the symmetric $p(2 \times 1)$ and (b) the $c(4 \times 2)$ reconstruction. (c) Spin model describing the arrangement of alternation of dimer buckling. Effective interaction parameters J_{\parallel} and J_{\perp} along and across the dimer rows are indicated. (d) STM image recorded at $T = 300 \text{ K}$, $U = -2.0 \text{ V}$, $I = 0.7 \text{ nA}$ (occupied states) exhibiting buckled dimers in the vicinity of a surface defect.

The bare dimerized Si(001) surface exhibits a rich hierarchy of structural motifs that minimize the surface free energy [41]. The dimer formation is facilitated by the energy minimization of the bulk-terminated Si surface, where each surface atom has two half-filled dangling bonds. This unstable structure results from the directional covalent bonds of the underlying diamond crystal structure. Each dimer is composed of two Si surface atoms bonded to each other, resulting in a two-fold periodicity along the dimer axis. As will be seen in Sec. V, the dimers form parallel dimer rows giving rise to a strong geometric and electronic anisotropy of the surface with a $p(2\times 1)$ unit cell as sketched in Fig. 1(a). The corresponding LEED pattern reflects the doubling of the periodicity by additional spots halfway between the integer order spots, as shown in Fig. 4(a). Each dimer reduces the number of half-filled dangling bonds by a σ -like bond resulting from the overlap of half-filled dangling bond orbitals as sketched in Fig. 1(a). This fully occupied σ -like bond reduces the lateral distance between the two Si surface atoms from 3.84 Å to 2.23 Å [42]. The associated bending of the backbonds from the top Si surface atoms by $\approx 20^\circ$ brings the two remaining dangling bonds almost parallel to each other, allowing for further energy reduction by forming a π -like bond. The energy gain of ≈ 1.8 eV per $p(2\times 1)$ unit cell due to the saturation of the dangling bonds overcompensates by far the energy cost of the unfavorable bending of the backbonds. Due to this large gain of energy the Si(001) surface remains dimerized up to temperatures of at least 1200°C [43].

The symmetric dimer, however, is unstable to lateral and vertical buckling and can further reduce its energy by Jahn-Teller distortion: one of the dimer atoms moves inward toward the bulk, the other outward toward the vacuum as sketched in Fig. 1(b) [20]. Such buckling does not require changes of bond lengths which are almost conserved while the bond angles change drastically until the dimer is tilted by 18° with respect to the surface plane [41, 44–49] as sketched in Fig. 1(b). This process is accompanied by a charge transfer of $\approx 0.1e_0$ (e_0 is the elementary charge) from the down-dangling bond D_{down} to the energetically more favorable s-like up-dangling bond D_{up} [50]. This charge transfer from the lower to the upper dangling bond causes the ionic character of the surface atoms. The repulsive force between equally charged dimer atoms induces an alternation of the dimer buckling direction along each dimer row. Each negatively charged up-atom is now surrounded by four positively charged down-atoms reducing the electrostatic repulsion between the ionic dangling bonds. Ramstad *et al.* used first-principles calculations to determine the reduction of surface energy

due to alternatively buckled dimers by another 50 meV/dimer [41].

There is still one degree of freedom left for the arrangement of the alternately buckled dimer rows. The registry of buckling in neighboring dimer rows could be either in-phase as for the asymmetric $p(2\times 2)$ reconstruction or phase-shifted by one lattice spacing along the dimer rows resulting in the $c(4\times 2)$ reconstruction as sketched in Fig. 1(b) and observed in LEED as shown in Fig. 4(b). Due to electrostatic interaction and minimization of surface stress, the $c(4\times 2)$ structure is slightly (by 3 meV/dimer according to the calculations of Ref. 41) more favorable than the $p(2\times 2)$ structure, where the buckling in adjacent dimer rows occurs in-phase. This is supported by LEED above ≈ 45 K, where only faint intensity of the $(1/2\ 1/2)$ spot was reported [32, 33, 51]. However, small portions of the surface may exhibit the $p(2\times 2)$ reconstruction in coexistence with the $c(4\times 2)$ reconstruction at very low temperatures below ≈ 45 K [51], where the long-range order of the buckled dimers in the $c(4\times 2)$ reconstruction can still be lifted locally by the creation and motion of anti-phase translational domain boundaries (so-called phasons) [52–54] and/or by electron doping by the probe [55–61].

Dąbrowski *et al.* determined an energy barrier of 90 meV between the asymmetric left- and right-tilted states of the $p(2\times 1)$ phase [49]. Their calculations exclude any metastable state as function of buckling angle, i.e., there exists no symmetric dimer configuration without buckling. At room temperature, however, the dimers appear as a symmetric $p(2\times 1)$ [Fig. 1(a)] in scanning tunneling microscopy (STM) due to fast dynamical flipping motion between left- and right-tilted configurations at a frequency of 10^{11} s^{-1} [49]. Figure 1(d) shows a room temperature STM image at negative sample bias, i.e., imaging the occupied states of the Si(001) surface. The $p(2\times 1)$ -reconstructed dimer rows are clearly visible. Dark areas represent missing dimer defects. In the vicinity of an extended defect the thermally activated flipping motion of the buckled dimers is quenched in two adjacent dimer rows, locally exhibiting the $c(4\times 2)$ reconstruction. The transition between the $c(4\times 2)$ ground state and the $p(2\times 1)$ reconstruction observed at room temperature is also described as an order-disorder transition.

III. FIRST-PRINCIPLES CALCULATIONS

A. DFT methods

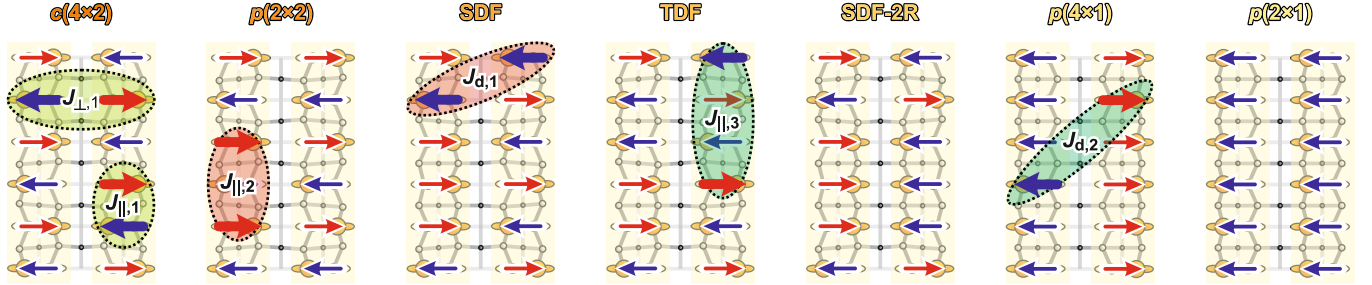


FIG. 2. **Schematics of dimer tilting patterns of the Si(001) surface.** Seven different dimer tilting patterns of the Si(001) surface were studied in DFT modeling to determine up to six interaction parameters between the Si dimers (denoted by the highlighted arrows in the ellipsoids). Here, SDF, TDF, and SDF-2R stand for single dimer flipped, twin dimers flipped (in one row), and single dimer flipped in adjacent rows, respectively. Heads and tails of arrows denote the up- and down-dangling bonds of the tilted surface Si dimers as introduced in Fig. 1(c).

Our goal is to describe the thermodynamics of the Si(001) surface by a lattice Hamiltonian. Since the potential energy surface of the Si dimers has two clearly distinct minima and a saddle point in between [16, 49, 62], it is appropriate to model the buckling angle by Ising spins $\sigma_{i,j} = \pm 1$ corresponding to the two buckling orientations 'right' or 'left' of the Si dimers as sketched in Fig. 1(c). The energetics of the Si(001) surface, including low-energy excitations of the Si dimer pattern, are described by a generalized anisotropic 2D Ising model on a rectangular lattice. We use DFT calculations as implemented in the Quantum Espresso (QE) simulation package [63] to determine the coupling parameters in this model. QE is a periodic DFT computational suite that implements plane waves for the expansion of electronic wave functions.

Here, we compare three different functionals to treat the exchange-correlation interactions of electrons, the local density approximation (LDA) as parametrized by Perdew and Zunger (PZ) [64], and the generalized gradient approximations (GGAs) in the parametrizations PBE [65] and PBEsol [66]. The ion-valence electron interactions are treated using norm-conserving pseudo-potentials of Hartwigsen-Goedecker-Hutter type [67] when PZ and PBE

exchange-correlation functionals are used, and an ultra-soft pseudo-potential [68] when the PBEsol functional is used. For geometry relaxation the convergence thresholds of the total energy and each component of forces on each atom were set at 0.1 meV and 1 meV/Å, respectively. The calculations were performed at $T = 0$ K.

For these calculations a (6×4) supercell of the Si(001) surface with two Si dimer rows was constructed with 8 Si atomic layers. The lateral dimensions of the supercell were set according to the bulk lattice constant of Si, which was determined individually for each functional. The supercell included a vacuum region of 15 Å to avoid artificial interactions between the slab and its image replicas normal to the surface. In addition, total energy calculations for fixed geometries were carried out for a plane-wave cut-off of 75 Ry, following a total energy convergence test of the cut-off energy. To carry out total energy integration over the Brillouin zone of the supercell, a Monkhorst-Pack mesh [69] of $3 \times 5 \times 1$ was used after fully examining the convergence of the total energy with respect to the size of the k -mesh. The dangling bonds of the bottom-most Si atoms were saturated using H atoms and the Si and H atoms in these layers were kept fixed throughout the geometry relaxation.

In the present work, seven different tilting patterns of the Si(001) surface were modelled in order to obtain the coupling constants of the lattice Hamiltonian, which, as will be shown, describes the short-ranged dimer interactions and their contributions to the total energy of the Si(001) surface. Figure 2 displays the modelled tilting patterns. Among the Si(001) surface tilting patterns, only the $p(2 \times 1)$ and $p(4 \times 1)$ reconstructions do not have an alternation of the buckling along a Si dimer row. As will be shown, this translational symmetry along the Si dimer row introduces an energy penalty that makes these two tilting patterns energetically less favorable. Also, according to previous experimental reports on the existence of domain boundaries (phasons) on the Si(001) surface [52], we modelled $c(4 \times 2)$ patterns in which the domain boundaries exist in one row due to flipping of a single dimer in one row (SDF) or two dimers in two adjacent rows (SDF-2R), see Fig. 2. We also included a tilting pattern with two domain boundaries formed by flipping of two dimers (TDF) in a single Si dimer row, see Fig. 2.

B. Lattice Hamiltonian

In early works [35, 70, 71], researchers included at least three short-range two-spin interactions $J_{\parallel,1}$, $J_{\perp,1}$ and $J_{d,1}$, along, across, and diagonal to the Si dimer rows in their Hamiltonians, see Fig. 2. Later, conditional longer-range multi-spin interactions (C_{V3} and C_{V4}) were added [47, 72], which contribute only when three or four adjacent dimers are tilted in the same direction, see the Appendix for a discussion. In addition, a second-nearest neighbor (NNN) interaction $J_{\parallel,2}$ as well as a four-spin plaquette interaction were first introduced by Ihm *et al.* [70], denoted as U and F in their Hamiltonian.

In this work, we demonstrate that it is sufficient to solely use two-spin interactions to account for the most important two-, three-, and four-dimer interactions within two dimer rows in our DFT model. However, as the correlations along the dimer rows are much stronger than across the dimer rows [36], in addition to the nearest-neighbor (NN) interactions we allow for NNN and third-nearest neighbor (NNNN) interactions in the direction along the dimer rows. Thus, the generalized Ising model Hamiltonian used here reads

$$\begin{aligned} \mathcal{H}_{\text{DFT}} = & -J_{\perp,1} \sum_{i,j} \sigma_{i,j} \sigma_{i+1,j} - \sum_{r=1}^3 J_{\parallel,r} \sum_{i,j} \sigma_{i,j} \sigma_{i,j+r} \\ & - \sum_{r=1}^2 J_{d,r} \sum_{i,j} \sigma_{i,j} (\sigma_{i+1,j+r} + \sigma_{i+1,j-r}) . \end{aligned} \quad (1)$$

In the direction across the dimer rows longer-ranging interactions than $J_{\perp,1}$ are neglected since they turned out to be reasonably small. For comparison with previous works, we also explored two approaches that simply add C_{V3} , or both C_{V3} and C_{V4} instead of $J_{\parallel,2}$, $J_{\parallel,3}$, and $J_{d,2}$. These results are summarized in the Appendix.

In the present work, seven dimer tilting patterns of the Si(001) surface with varying thermal stability were studied, see Fig. 2. Defining the renormalized effective NN couplings [36]

$$J_{\parallel} = J_{\parallel,1} - J_{\parallel,2} + J_{\parallel,3} , \quad (2a)$$

$$J_{\perp} = J_{\perp,1} - 2J_{d,1} + 2J_{d,2} , \quad (2b)$$

the coupling parameters of the Hamiltonian given in Eq. (1) are determined by solving a system of linear equations corresponding to the tilting patterns considered. Subtracting the

energy of the reference ground state $c(4\times 2)$, we find

$$E_{c(4\times 2)} = 0, \quad (3a)$$

$$E_{p(2\times 2)} = -24J_{\perp}, \quad (3b)$$

$$E_{\text{SDF}} = -4(J_{\parallel} + J_{\perp}), \quad (3c)$$

$$E_{\text{TDF}} = -8(J_{\parallel} + J_{\perp} - \frac{1}{2}J_{\parallel,1}), \quad (3d)$$

$$E_{\text{SDF-2R}} = -8(J_{\parallel} + J_{\perp} - J_{\perp,1}), \quad (3e)$$

$$E_{p(4\times 1)} = -24(J_{\parallel} + J_{\perp} - J_{\perp,1} + J_{\parallel,2}), \quad (3f)$$

$$E_{p(2\times 1)} = -24(J_{\parallel} + J_{\perp} + 2J_{\text{d},1} + J_{\parallel,2}), \quad (3g)$$

where the quantities on the left sides are the DFT total energies of the dimer tilting patterns in the (6×4) supercell.

C. DFT results on lattice Hamiltonian

Using all seven structures calculated by DFT, we are able to fit a lattice Hamiltonian with six interaction parameters. From this starting point, it is possible to construct a more compact Hamiltonian with only two parameters by using the renormalized interactions J_{\perp}

TABLE I. **DFT results on energetics of the tilting patterns.** Relative energies of the tilting patterns of the (6×4) supercell obtained using different exchange-correlation functionals (in combination with appropriate pseudo-potentials). The energies (in meV) are given relative to the total energy of the $c(4\times 2)$ reconstruction.

Tilting pattern	LDA	PBE	PBEsol
$c(4\times 2)$	0.0	0.0	0.0
$p(2\times 2)$	37.9	12.3	16.3
SDF	105.7	131.4	111.3
TDF	103.2	123.9	109.8
SDF-2R	242.3	306.8	249.9
$p(4\times 1)$	1169.1	1293.6	1220.1
$p(2\times 1)$	858.3	942.3	890.5

TABLE II. **DFT results on interaction energies.** Interaction energies are given in meV. For each functional, the left columns are determined from the three energies Eqs. (3a-3c), with $J_{\parallel,2} = J_{\parallel,3} = J_{d,1} = J_{d,2} = 0$, while the middle columns result from the five energetically lowest structures Eqs. (3a-3e), with $J_{\parallel,3} = J_{d,2} = 0$. Finally, the right columns are the result of all structures with the full Hamiltonian Eq. (1). Note that the resulting renormalized effective NN couplings $J_{\parallel,\perp}$ are equal in all cases. T_c is derived by Eq. (6) using the values for $J_{\parallel,\perp}$.

Eqs.	LDA [64]			PBE [65]			PBEsol [66]		
	(3a-3c)	(3a-3e)	(3a-3g)	(3a-3c)	(3a-3e)	(3a-3g)	(3a-3c)	(3a-3e)	(3a-3g)
$J_{\parallel,1}$	-24.9	-27.1	-27.1	-32.3	-34.7	-34.7	-27.1	-28.2	-28.2
$J_{\parallel,2}$	0	-2.2	-16.6	0	-2.4	-14.0	0	-1.0	-16.5
$J_{\parallel,3}$	0	0	-14.4	0	0	-11.6	0	0	-15.4
J_{\parallel}	-24.9			-32.3			-27.1		
$J_{\perp,1}$	-1.6	3.9	3.9	-0.5	5.5	5.5	-0.7	3.4	3.4
$J_{d,1}$	0	2.7	3.6	0	3.0	3.8	0	2.0	3.6
$J_{d,2}$	0	0	0.9	0	0	0.8	0	0	1.6
J_{\perp}	-1.6			-0.5			-0.7		
J_{\parallel}/J_{\perp}	15.7			63.1			40.0		
T_c (K)	228.4			210.5			195.9		
a_{lat} (Å)	5.38			5.46			5.43		

and J_{\parallel} , cf. Eqs. (2). Alternatively, one can start by constructing a Hamiltonian emphasizing only the lowest-lying structures, those shown in Fig. 2(a-e). Using these five structures and using Eqs. (3a) to (3e) one obtains a Hamiltonian with four interaction parameters, two along the dimer row and two across the dimer row or in the diagonal direction. Again, the renormalization procedure defined by Eqs. (2) can be applied to obtain J_{\perp} and J_{\parallel} . Interestingly, identical effective interactions are obtained. Finally, we employed the $p(2 \times 2)$, $c(4 \times 2)$ and the single-dimer excitation SDF to directly obtain the two interaction parameters J_{\perp} and J_{\parallel} using Eqs. (3a) to (3c). Again, we obtain the same numerical values as from the

renormalization of the more complex Hamiltonians. This provides strong evidence that a two-parameter Hamiltonian with effective interactions is suitable to correctly describe the phase transition on the dimerized Si(001) surface. Lattice Hamiltonians including more long-range interactions may still be useful in providing microscopic understanding. However, due to the alternating sign of the dimer buckling, the more long-ranged interactions, entering with positive and negative signs in Eqs. (2), tend to cancel each other out. Thus, it is possible to 'condense' these interactions into a compact Hamiltonian with only NN interactions without loss of accuracy. The numerical results of our DFT calculations are summarized in Tables I and II for the functionals used.

It is found that the interaction $J_{\parallel} < 0$ is strongest along the Si dimer rows, in support of a pronounced anticorrelation between the tilt angles of adjacent dimers along a row. Compared to $J_{\parallel,1}$, the NNN interaction $J_{\parallel,2}$ is found to be considerably smaller. Therefore it seems justified to neglect this interaction in a first analysis. Considering the even longer ranging NNNN interaction $J_{\parallel,3}$ does not affect the values of $J_{\parallel,1}$, but interestingly $J_{\parallel,2}$ is renormalized. Still, the sum of both remains the same as well as the value of J_{\parallel} . Except for the case when only Eqs. (3a)-(3c) are considered, the interactions between the dimer rows, $J_{\perp,1}$, $J_{d,1}$ and $J_{d,2}$, are found to have positive signs, but their combination J_{\perp} [Eq. (2b)] turns out to be negative in all cases, showing that an alternating tilt angle of the dimers is also preferred across the dimer rows.

Comparing the results obtained with the different DFT functionals, one notes that PBE yields consistently the largest values for J_{\parallel} , while LDA yields the smallest values. The opposite finding holds for J_{\perp} . These trends correlate with the lattice constant predicted by the functionals: While PBE overestimates the lattice constant a_{lat} of bulk silicon (DFT value 5.46 Å vs. experimental value 5.43 Å) and LDA underestimates it (5.38 Å), the PBEsol functional gives the most accurate value (5.43 Å).

We argue that getting the lattice constant right (and setting up the slab calculations with the theoretically determined lattice constant for each functional) has a crucial impact on the surface stress. It has been demonstrated experimentally that the Si(001) surface is under anisotropic surface stress [73]. For a DFT calculation to describe the experimental stress state, it is important to reproduce the experimental lattice constant, since this defines the boundary condition for the elastic problem from which the surface stress results. The fact that the Si dimers prefer to buckle alternately is an indication that the surface attempts

to reduce the local surface stress [74]. Hence, the interaction parameters expected to be highly sensitive to stress, or equivalently to strain, as recently demonstrated by means of DFT calculations [72].

An intuitive picture of the energetics of the Si(001) surface may be obtained best by looking at the energy differences. The energy gain for the $c(4\times 2)$ reconstruction over the $p(2\times 2)$ reconstruction obtained in our calculations is 1.4 meV/dimer using the PBEsol functional (cf. Table I). In comparison, Ramstad *et al.* derived a value of (3 ± 13) meV/dimer in their LDA calculations [41], while in the PBE calculations of Xiao *et al.* [72] only an energy gain of 0.1 meV/dimer was obtained. These scattered data indicate that such calculations depend on subtle details and choice of the proper functional and that the computational error is of the same order of magnitude as the results. Irrespective of the DFT functional used, our results confirm that the $c(4\times 2)$ reconstruction is indeed the most stable reconstruction for the dimerized Si(001) surface at $T = 0$ K.

To locate transition states we used the Climbing-Image Nudged Elastic Band (CI-NEB) [75] method. Two different types of processes were considered: the creation of a phason-antiphason pair by flipping one dimer in a perfect $p(2\times 2)$ reconstruction of Si(001), and the barrier for moving an isolated phason by one lattice distance along the Si dimer row. For the latter case, a (5×2) supercell of Si(001) was constructed and the flipping of a single dimer was modelled. A total of eight images were considered to sample the reaction path of the Si dimer flipping. Starting from the $p(2\times 2)$ reconstruction, for flipping of a Si dimer the barrier energies of 110, 150, and 74 meV are obtained using the LDA, PBE, and PBEsol functionals, respectively. Since the thermal energy equivalent to the measured (and calculated) T_c is small compared to the barrier energies, crossing the barrier is a rare event, and thus the thermodynamic modelling with $\sigma_{i,j} = \pm 1$ is justified, as any intermediate tilting angles contribute negligibly to a thermal average.

Finally, we identify the elementary excitations of the $c(4\times 2)$ ground state. Structurally, the simplest excitation is flipping of a single dimer from its equilibrium tilting position to the opposite tilting. This situation is depicted as the SDF state in Fig. 2. The excitation energy is given by the energy difference between the SDF state and the ground state and can be calculated from Eq. (3c). Our calculations yield an excitation energy on the order of 100 meV for all three functionals (cf. Table I). The energy barriers for such a transition, i.e., for creating a phason-antiphason pair, are 165 meV (LDA), 129 meV (PBEsol), and 209 meV

(PBE), respectively. Interestingly, the excitation of the SDF state is energetically not the lowest possible excitation of the system. Our calculations show that the TDF state (where two adjacent dimers are flipped along the dimer rows) is energetically slightly below the SDF state (cf. Table I). This indicates that a phason and an antiphason on adjacent lattice sites tend to repel each other. It should also be noted that the energy per dimer for the $p(2\times 2)$ reconstruction is lower than for the SDF and TDF states. However, such non-local collective excitation of the entire surface is unlikely to occur at low temperatures.

D. Surface stress

The surface stress tensor for each tilting pattern of the Si(001) surface is obtained from the (6×4) supercell stress tensor as

$$\sigma_{\alpha\beta}^{\text{surf}} = c(\sigma_{\alpha\beta}^{\text{sc}} - \sigma_{zz}\delta_{\alpha\beta} - \frac{1}{2}\sigma_{\alpha\beta}^{\text{sc,H}}), \quad (4)$$

where $c = 30 \text{ \AA}$ is the dimension of the supercell normal to the surface. $\sigma_{\alpha\beta}^{\text{sc,H}}$ is the supercell surface stress of the Si surface slab passivated on both sides by H atoms. Including such a term ensures that the contribution of H atoms (at the bottom of the Si slab) to the stress is well excluded. Also, the presence of σ_{zz} in the above expression ensures that the residual non-zero diagonal surface stress component perpendicular to the surface vanishes to zero. The numerical $\sigma_{zz} = 0$ satisfies the physical requirement of zero z stress for the slab model [74]. The components of the surface stress tensor for each tilting pattern are calculated as $\sigma_{xx}^{\text{surf}} \mapsto \sigma_{\parallel}$ and $\sigma_{yy}^{\text{surf}} \mapsto \sigma_{\perp}$ for the respective directions along and across the dimer rows (cf. Table III). Finally, the stress anisotropy $\Delta\sigma = \sigma_{\perp} - \sigma_{\parallel}$ of the tilting patterns is used to quantify the magnitude of the difference between the surface stress tensor components across and along the Si dimer row. It should be noted that for the $p(4\times 1)$ and $p(2\times 1)$ reconstructions σ_{\parallel} becomes negative, i.e., a compressive stress arises which makes both patterns energetically unfavorable compared to the other reconstructions (cf. Table I). This is in good agreement with experimental [76] and theoretical [77] works, which suggest tensile and compressive stresses across and along the dimer rows, respectively, for Si(001) with $p(2\times 1)$ domains formed at 730°C temperature. Also across the dimer rows the Si surface is subject to tensile stress σ_{\perp} , which remains almost the same for each tilting pattern. This is because it is an individual property of the dimer bond and its length does not change

TABLE III. **DFT results on surface stress.** Surface stress $\sigma_{\parallel,\perp}$ (in $\text{meV}/\text{\AA}^2$) of the tilting patterns of the (6×4) supercell obtained using different exchange-correlation levels of theory. Negative (positive) signs denote compressive (tensile) stress.

Tilting pattern	LDA		PBE		PBEsol	
	σ_{\perp}	σ_{\parallel}	σ_{\perp}	σ_{\parallel}	σ_{\perp}	σ_{\parallel}
$c(4\times 2)$	76.8	45.5	109.2	44.8	82.4	43.3
$p(2\times 2)$	77.8	47.0	110.9	46.1	83.5	45.0
SDF	73.3	29.2	107.5	30.3	79.0	26.2
TDF	75.3	33.2	108.4	33.1	80.1	30.3
SDF-2R	79.1	3.5	105.9	11.7	76.6	5.0
$p(4\times 1)$	84.6	-23.4	108.5	-19.3	79.0	-24.9
$p(2\times 1)$	77.6	-6.0	107.2	-8.7	82.2	-8.5

dramatically upon different reconstructions of the Si(001) surface.

Our results show that the stress anisotropy $\Delta\sigma$ becomes smallest (nearly $39\text{ meV}/\text{\AA}^2$ using the PBEsol functional) when Si dimers form the $c(4\times 2)$ and $p(2\times 2)$ tilting patterns. In contrast, for tilting patterns with translational symmetries, $p(4\times 1)$ and $p(2\times 1)$, the surface stress anisotropy becomes very large (104 and $91\text{ meV}/\text{\AA}^2$) because the surface is under compressive stress along the Si dimer row. Our results are in good agreement with those of previous theoretical [74, 78] and experimental works [79].

Looking at the stress anisotropy at different levels of DFT theory gives us clue to correlations between the stress anisotropy and the coupling constant ratio J_{\parallel}/J_{\perp} with the DFT functionals. For the $c(4\times 2)$ reconstruction the ratio J_{\parallel}/J_{\perp} amounts to 15.7, 63.1, and 40.0 for the LDA, PBE and PBEsol functionals, respectively (cf. Table I). From Table III we derive for the stress anisotropy values of 31.3, 64.4, and $39.1\text{ meV}/\text{\AA}^2$ for LDA, PBE and PBEsol functionals, respectively. Thus, a good correlation can be seen between the stress anisotropy and the coupling constant ratio J_{\parallel}/J_{\perp} as well as for the lattice constant (cf. Table I). Therefore, there is a clear correspondence between the stress anisotropy and the coupling constant ratio.

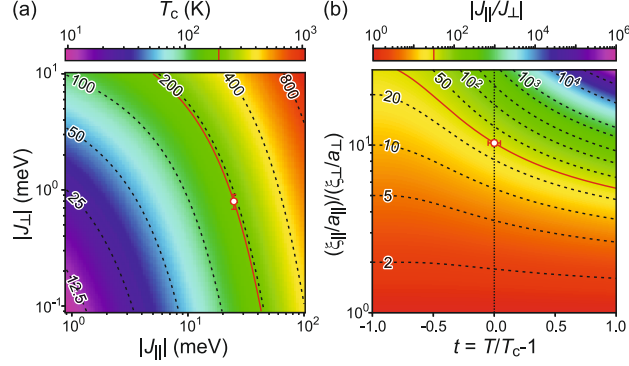


FIG. 3. **Energetics of the anisotropic 2D Ising model.** (a) Critical temperature T_c as a function of the effective NN coupling constants J_{\parallel} and J_{\perp} . (b) Temperature and correlation length ratio dependence of the coupling energy ratio $|J_{\parallel}/J_{\perp}|$ derived from Eq. (8). Eq. (6) holds at the black dotted line with $t = 0$ where the relation for $(\xi_{\parallel}^+/a_{\parallel})/(\xi_{\perp}^+/a_{\perp})$ simplifies to Eq. (10). Red solid lines and the data points indicate results for $T_c = (190.6 \pm 0.4_{\text{stat}} \pm 9.6_{\text{sys}})$ K in (a) and $J_{\parallel}/J_{\perp} = 31.2 \pm 3.8_{\text{stat}}$ in (b) as derived from the experiment.

IV. ANISOTROPIC 2D ISING MODEL

In the further analysis of the order-disorder phase transition and of the experimental data, we choose to model the system based on the well-known anisotropic 2D Ising model on a rectangular lattice with the Hamiltonian

$$\mathcal{H}_I = - \sum_{i,j} (J_{\parallel} \sigma_{i,j} \sigma_{i,j+1} + J_{\perp} \sigma_{i,j} \sigma_{i+1,j}) , \quad (5)$$

where J_{\parallel} is the effective NN coupling along the dimer row, while J_{\perp} is the effective NN coupling between adjacent rows. In advantage over more complex models, the 2D Ising model is accessible to an analytical solution [39], and the well-known scaling laws can be used as a basis for fitting experimental data. By analyzing the spot profiles in an electron diffraction experiment along the two directions along and across the dimer rows, the effective NN interaction parameters $J_{\parallel,\perp}$ can be determined experimentally, whereas it is difficult to extract signatures of any more long-ranged interaction parameters from such experimental data.

According to the analytical solution of the 2D Ising model by Onsager [39], the system

exhibits a second-order phase transition at the critical temperature T_c determined by [80]

$$\sinh\left(\frac{2|J_{\parallel}|}{k_B T_c}\right) \sinh\left(\frac{2|J_{\perp}|}{k_B T_c}\right) = 1. \quad (6)$$

A false-color plot of the solution of Eq. (6) is shown in Fig. 3(a) together with the results of the experiment [36].

The spin-spin correlation function $\langle \sigma_{i,j} \sigma_{k,l} \rangle$ decays exponentially on a length scale given by the anisotropic correlation length ξ_{δ} in direction $\delta \in \{\parallel, \perp\}$. Above (below) T_c , the correlation function asymptotically decays to zero (a constant value); characteristics of a second-order phase transition.

In the vicinity of the phase transition, however, the system exhibits universal critical behavior, i.e., quantities such as the correlation length $\xi_{\delta}(t)$, the order parameter $\Psi(t)$, or the susceptibility $\chi(t)$ behave asymptotically as power laws of the reduced temperature $t = T/T_c - 1$,

$$\Psi(t) \simeq \Psi^{-} (-t)^{\beta}, \quad (7a)$$

$$\chi(t) \simeq \chi^{\pm} |t|^{-\gamma}, \quad (7b)$$

$$\xi_{\delta}(t) \simeq \xi_{\delta}^{\pm} |t|^{-\nu}. \quad (7c)$$

Here, Ψ^{-} , χ^{\pm} and ξ_{δ}^{\pm} are non-universal amplitudes above and below T_c , while the critical exponents have the values $\beta = 1/8$, $\gamma = 7/4$ and $\nu = 1$ for the universality class of the 2D Ising model. These exponents can accurately describe the behavior of the system close to the critical temperature. Indeed, χ generally corresponds to fluctuations that are strong near the critical temperature T_c .

Above T_c , the correlation lengths ξ_{δ} in the anisotropic 2D Ising model are given by [40, 81]

$$\frac{\xi_{\delta}(T)}{a_{\delta}} \stackrel{T \geq T_c}{=} \left[\ln \coth \left(\frac{|J_{\delta}|}{k_B T} \right) - \frac{2|J_{\bar{\delta}}|}{k_B T} \right]^{-1}, \quad (8)$$

where $a_{\parallel} = 3.84 \text{ \AA}$ is the Si(001) surface lattice parameter, and $a_{\perp} = 2a_{\parallel}$, while $\bar{\delta}$ denotes the direction perpendicular to δ . With Eq. (6) and the correlation length ratio $(\xi_{\parallel}/a_{\parallel})/(\xi_{\perp}/a_{\perp})$ [which holds above and below T_c , see Fig. 3(b)] derived from Eq. (8), the renormalized effective NN couplings J_{δ} of the Si dimers/spins along and across the dimer rows can be derived [36]: An expansion of Eq. (8) around T_c from Eq. (6) yields the correlation length amplitudes Eq. (7c) above T_c ,

$$\frac{\xi_{\delta}^{+}}{a_{\delta}} = \left[\frac{2|J_{\delta}|}{k_B T_c} \sinh \left(\frac{2|J_{\bar{\delta}}|}{k_B T_c} \right) + \frac{2|J_{\bar{\delta}}|}{k_B T_c} \right]^{-1}, \quad (9)$$

from which one can deduce a simple relation between the effective NN couplings J_δ and the ratio of correlation length amplitudes,

$$\frac{\xi_\delta^+/a_\delta}{\xi_\delta^+/a_{\bar{\delta}}} = \sinh\left(\frac{2|J_\delta|}{k_B T_c}\right), \quad (10)$$

such that we can determine the anisotropic renormalized effective NN couplings J_δ solely from the correlation length amplitude ratio [82]. Note that the signs of J_δ must be determined from the diffraction analysis below.

In a diffraction experiment we have access to these quantities by evaluating the spot intensity and its shape. For $T > T_c$, the diffraction pattern consists of Lorentzian peaks whose widths $\text{FWHM}_{L,\delta}$ are proportional to the inverse correlation lengths ξ_δ^{-1} , while their intensity I_L is proportional to the susceptibility χ . For $T < T_c$, the diffraction pattern consists of Lorentzian peaks just as for $T > T_c$, but in addition, there are delta peaks whose intensity I_G scales with the absolute square of the order parameter $|\Psi|^2$. Experimentally, all peaks are additionally broadened by the instrumental response function, i.e., a Gaussian function with constant FWHM independent of temperature.

V. EXPERIMENT

A. Experimental methods

We followed the order-disorder phase transition by means of SPA-LEED which combines high resolution in reciprocal space with superior signal-to-noise ratio [83, 84]. The experiments were performed under ultrahigh vacuum (UHV) conditions at a base pressure $p < 2 \times 10^{-10}$ mbar in order to ensure very low surface contamination by residual gas adsorption. The Si(001) sample (miscut $< 0.2^\circ$) was mounted on a cryostat for sample cooling with liquid nitrogen. Direct current was applied to heat the sample for degassing at 600°C and subsequent flash-annealing at $T > 1200^\circ\text{C}$ for 5 s with the pressure remaining in the 10^{-10} mbar regime. The temperature was monitored during annealing with an IMPAC IGA10 pyrometer. Subsequently, the sample was cooled to 78 K in less than 5 min. Using the built-in resistive heater of the cryostat, the sample was heated from 78 K to 400 K at a rate of 10 K/min while the sample temperature was measured with a Pt100 Ohmic sensor. The systematic error in temperature determination is in the order of ± 10 K while the statistical error is less than ± 1 K. At the same time spot profiles through the (00) spot,

$p(2\times 1)$ spots and $c(4\times 2)$ spots were continuously taken by SPA-LEED at an electron energy of $E = 112\text{ eV}$. The transfer width of our SPA-LEED was larger than 320 \AA . The probing electron beam can induce disorder in the $c(4\times 2)$ structure [34, 56–58]. We confirmed that this is not the case in our study because the beam current was kept as low as possible and is much smaller than in other optical LEED experiments. Scanning tunneling microscopy (STM) images were taken at room temperature in another chamber under UHV conditions.

B. Experimental results

The change of the surface structure upon the Si(001)’s order-disorder phase transition is clearly seen in the LEED patterns shown in Fig. 4 and taken at 300 K and 80 K, i.e., above and below the critical temperature, respectively. The diffraction pattern recorded at 300 K [Fig. 4(a)] exhibits sharp diffraction spots and a low background reflecting the low step density and low defect and/or adsorbate density. The pattern is composed of an incoherent superposition of two distinct $p(2\times 1)$ patterns originating from the 90° -rotated dimer rows arrangement on adjacent terraces. The two-fold periodicity in the diffraction pattern refers to the direction across the dimer rows, while the $\times 1$ periodicity is along the dimer rows [cf. Fig. 1(a), Fig. 4(a)]. From the FWHM (full width at half maximum) of the (00) spot, we determined that the terrace width was larger than 50 nm. The streaklike intensity centered at the quarter-integer order spot positions is visible even far above the critical temperature [32] and is indicative of fluctuations of the dimers, i.e., activation of diffusive phase defects in between $p(2\times 1)$ domains (phasons and antiphasons) [6, 52]. The faint intensity at the $(1/2\ \overline{1/2})$ position (see left panel in Fig. 6) at 50 %SBZ (surface Brillouin zone [$100\text{ \%SBZ} = 2\pi/(3.84\text{ \AA})$]) can originate either from the incoherent overlap of the streaklike intensities of surrounding $c(4\times 2)$ spots and/or from local $p(2\times 2)$ reconstruction sites. We estimate from the fits to the line profiles shown in Fig. 6 that the surface exhibits almost no sites of the latter at any temperature in the investigated range between 78 K and 400 K.

The diffraction pattern recorded at 80 K [Fig. 4(b)] exhibits additional sharp spots at those of the quarter-integer order positions belonging to a $c(4\times 2)$ reconstruction. The streaklike intensity is still present. Again, this pattern is composed of an incoherent superposition of two 90° -rotated $c(4\times 2)$ patterns. Thus, the surface structure has undergone

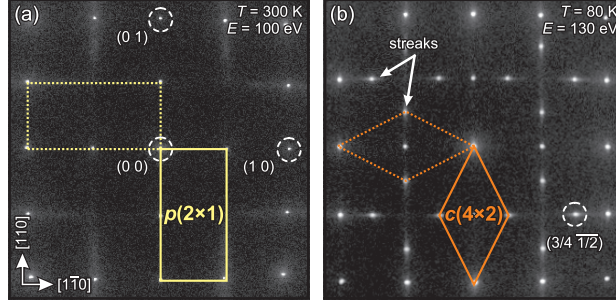


FIG. 4. **SPA-LEED patterns.** Patterns were taken at (a) $T = 300$ K and (b) $T = 80$ K, respectively. Primitive unit cells of the $p(2 \times 1)$ and $c(4 \times 2)$ reconstructions are indicated by the yellow rectangles and orange rhombi, respectively. Additional to the spots streaklike intensity is found centered at the $(3/4 \ 1/2)$ spots.

a phase transition to a $c(4 \times 2)$ reconstruction with two alternatively buckled dimers per centered unit cell, as sketched in Fig. 1(b).

For a quantitative analysis, spot intensity profiles in the temperature range 78-400 K were taken for several diffraction spots. Line profiles through the (00) spot and the half-integer order spots exhibit sharp Gaussian-shaped spots reflecting the long-range order of the surface [cf. insets of Fig. 5(d,e)]. The FWHM of these spots [see Fig. 5(d,e)] exhibits no temperature dependence. From the sharpest spot, i.e., the $(1 \ 1/2)$ spot, we determined the instrumental resolution of 1.07 %SBZ.

The Debye-Waller effect at temperature T

$$I(T) = I_0 \cdot e^{-\frac{1}{3} \langle \mathbf{u}^2 \rangle \cdot \Delta \mathbf{K}^2} \quad (11)$$

for the normalized spot intensity $I(T)/I_0$ with isotropic mean squared vibrational motion $\langle \mathbf{u}^2 \rangle$ of the atoms and momentum transfer $\Delta \mathbf{K}$ at almost vertical incidence of $90^\circ - \beta/2 = 86.5^\circ$ ($\beta = 7^\circ$ is the angle between electron gun and channeltron of the instrument [84]) was employed to disentangle the intensity drop due to the vibrational motion of the atoms and the contributions of the order-disorder phase transition for the peak intensities. Thus, in the framework of the Debye model the peak intensity for temperatures below the Debye temperature Θ_D is given by

$$I(T) = I_0 \cdot \text{DW}(T), \quad (12a)$$

where

$$\text{DW}(T) \approx \exp \left[\frac{\gamma}{\Theta_D} \left(1 + \frac{2}{3} \left[\frac{\pi T}{\Theta_D} \right]^2 \left[1 - e^{\left(1 - \frac{\pi^2}{6}\right) \frac{\Theta_D}{T}} \right] \right) \right] \quad (12b)$$

is the approximated Debye-Waller factor for $T \leq \Theta_D$ with

$$\gamma = -\frac{3\hbar^2 \Delta \mathbf{K}^2}{4m_{\text{Si}} k_B} \quad (12c)$$

and (for SPA-LEED)

$$\Delta \mathbf{K}^2 = \frac{4m_e}{\hbar^2} (1 + \cos \beta) E, \quad (12d)$$

where m_{Si} is the mass of the Si atoms.

The peak intensities of the relevant spots are plotted in Fig. 5(a). The intensities of the (00) and half-integer order spots [blue and green data points in Fig. 5(a)] decrease with increasing temperature which is explained through a simple Debye-Waller behavior. Their respective Debye temperatures of $\Theta_D = (474 \pm 7_{\text{stat}})$ K for the (00) spot [85] and $\Theta_D = (601 \pm 4_{\text{stat}})$ K for the half-integer order spots are determined using Eq. (12) [solid black curves in Fig. 5(a)]. However, the peak intensity of the quarter-integer order spot ($3/4 \overline{1/2}$) (red data points) clearly deviates from the Debye-Waller behavior as it is strongly affected by the phase transition. The drop in intensity at $T \approx 200$ K reflects the expected behavior for an order-disorder phase transition.

Figure 5(b) depicts the integrated intensity of the ($3/4 \overline{1/2}$) spot. Since the integrated intensity exhibits a small drop from the expected Debye-Waller behavior around the critical temperature, the fitting of the spot profile may still be affected by the critical behavior of the phase transition. We have therefore plotted a family of curves describing possible Debye-Waller behaviors using Eq. (12) for a range of Debye temperatures from $\Theta_D = 325$ K to 500 K. The best fit to the data is obtained for $\Theta_D = (391 \pm 7_{\text{stat}})$ K which is in reasonable agreement with the values obtained for the other spots. In addition, the thermal diffuse background intensity of the diffraction pattern shows an increase with temperature [Fig. 5(c)] as expected from Debye-Waller theory [84]. The corresponding Debye-Waller fit yields $\Theta_D = (367 \pm 108_{\text{stat}})$ K.

The quantitative investigation of the phase transition is employed through a detailed spot profile analysis of the ($3/4 \overline{1/2}$) spot. Using line profiles, both across (along the $[1\overline{1}0]$

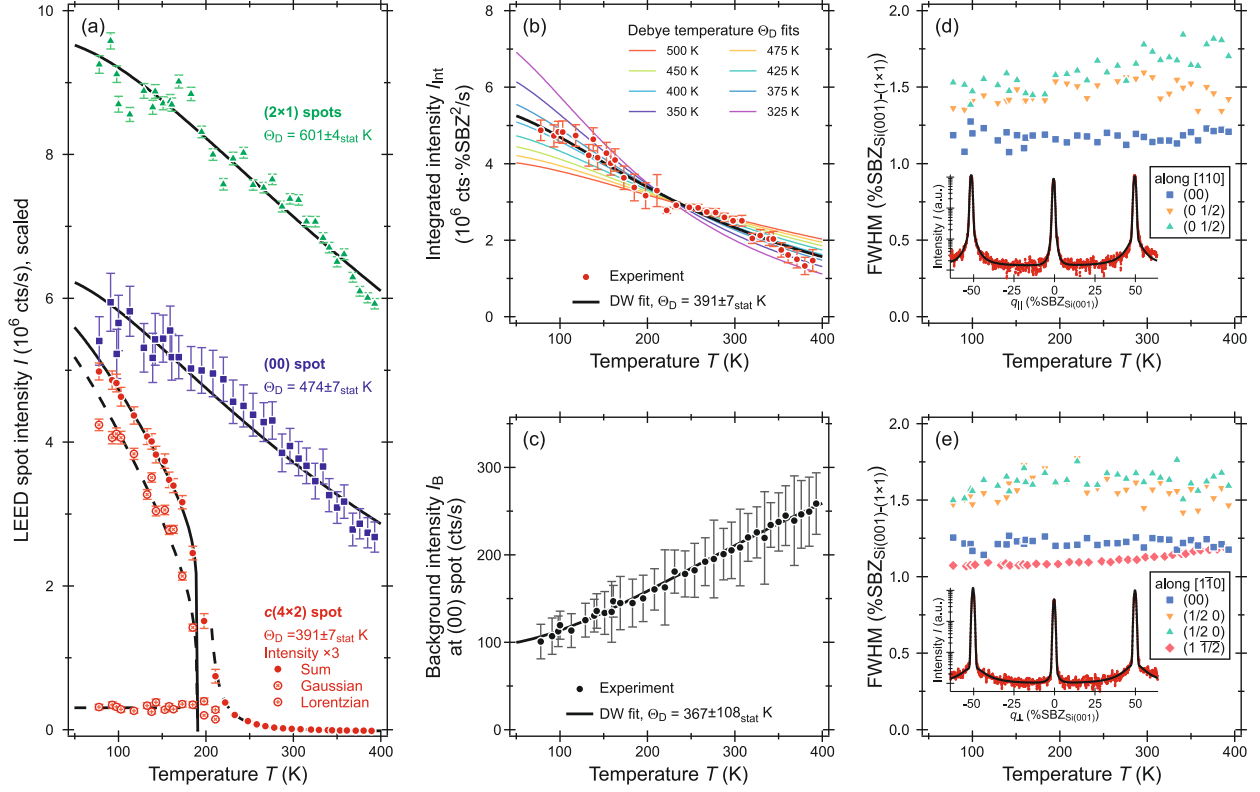


FIG. 5. **Temperature dependence of diffraction spots.** (a) Scaled LEED spot intensities I of the (00) spot, half-integer order spots and the $(3/4 \ 1/2)$ spot (shown with its Gaussian and Lorentzian contributions). The spot intensity decreases with increasing temperature due to the Debye-Waller effect according to Eq. (12). Debye temperatures are indicated. The $(3/4 \ 1/2)$ spot clearly deviates from simple Debye-Waller behavior as its intensity is affected by the order-disorder phase transition. (b) The integrated intensity I_{int} of the $(3/4 \ 1/2)$ spot drops as function of temperature due to the Debye-Waller effect according to Eq. (12) without being affected by the phase transition. Colored solid lines indicate the expected intensity drop due to the Debye-Waller effect for various Debye temperatures Θ_D between 325 K and 500 K. The black solid line depicts the best fit with $\Theta_D = (391 \pm 7_{\text{stat}})$ K. (c) Intensity of the homogeneous thermal diffuse background I_B and corresponding Debye-Waller fit yielding $\Theta_D = (367 \pm 108_{\text{stat}})$ K. (d,e) FWHMs (uncorrected for instrumental resolution) of the (00) spot and half-integer order spots along the $[110]$ and $[1\bar{1}0]$ direction, respectively. Insets show line profiles (red dots) and corresponding fits (black lines) through the (00) spot and neighboring half-integer order spots at $T = 78$ K.

direction, left panel in Fig. 6) and along (along the [110] direction, right panel in Fig. 6) the Si dimer rows, the temperature dependence of the spot profiles has been recorded. The spot profiles consist of a sharp central spike, a broad diffuse part, and background intensity. In accordance with the 2D Ising model and Refs. 32 and 33, the data were therefore fitted by a combination of an intense Gaussian-shaped contribution (sharp central spike) with peak intensity $I_G(t)$ and full width at half maximum $\text{FWHM}_{G,\delta}$ and a broad less intense Lorentzian-shaped contribution (broad diffuse part) with peak intensity $I_L(\mathbf{q}_0, t)$ and full width at half maximum $\text{FWHM}_{L,\delta}(t) = 2\pi/\xi_\delta(t)$, respectively, where we consider a spot at reciprocal lattice vector \mathbf{q}_0 , with $\mathbf{q} = (q_\parallel, q_\perp)$. Such a line profile in direction δ is therefore described by

$$I(q_\delta, t) = \delta(q_\delta - q_{0,\delta})I_G(t) + I_L(q_\delta, t), \quad (13a)$$

with asymptotic scaling forms after Debye-Waller correction

$$I_G(t) \simeq A_G^- (-t)^{2\beta}, \quad (13b)$$

$$I_L(q_\delta, t) \simeq A_L^\pm(y_\delta^\pm) |t|^{-\gamma}, \quad (13c)$$

near T_c , where we introduced the dimensionless scaling variable [86]

$$y_\delta^\pm = \xi_\delta^\pm |t|^{-\nu} \frac{q_\delta - q_{0,\delta}}{2\pi}. \quad (13d)$$

Here, $I_G(t)$ describes the sharp central δ -spike proportional to the square of the order parameter $\Psi(t)$ from Eq. (7a) and follows a power law with exponent $2\beta = 1/4$ and amplitude A_G^- below T_c . Accordingly, $I_L(q_\delta, t)$ is the broad diffuse part of the spot profile, whose height is proportional to the susceptibility $\chi(t)$ from Eq. (7b) and scales with an exponent of $\gamma = 7/4$, while its width scales anisotropically with the inverse correlation lengths $\xi_\delta(t)$ from Eq. (7c). The corresponding Lorentzian scaling function is denoted $A_L^\pm(y_\delta^\pm)$ and will be discussed at the end of this section.

To account for the instrumental response function of the SPA-LEED, a pseudo-Voigtian function (sum of a Lorentzian and a Gaussian peak with the minimum Gaussian FWHM of the sharpest spot, i.e., the $(1 \sqrt{1/2})$ spot as a measure of the instrumental response) was used to fit the Lorentzian contribution. Accordingly, also the Gaussian contribution is broadened by the instrumental response function. The fit to the data is superimposed on the line profiles in Fig. 6 as red curves.

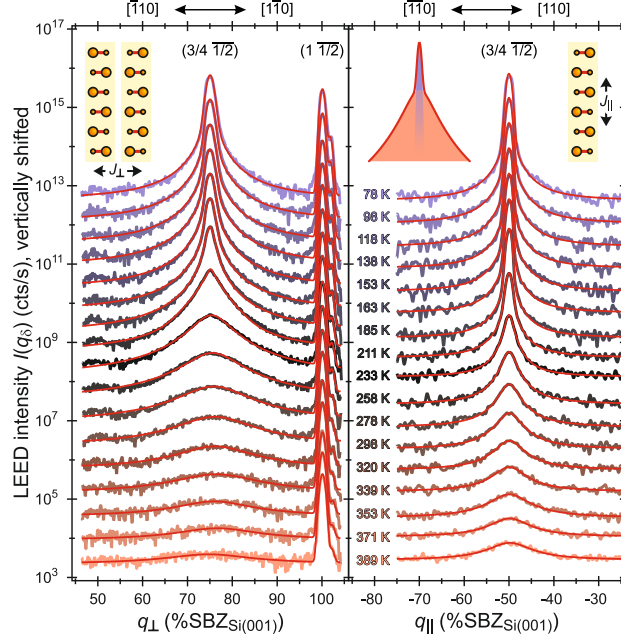


FIG. 6. **Temperature dependence of line profiles through the $(3/4 \overline{1/2})$ spot.** Profiles through the center of the spot were recorded in the directions across (left panel) and along (right panel) the dimer rows. Data are plotted as bluish to reddish lines while the fit to the data is given by the solid red lines, see also Eq. (13). For better visibility the experimental data is Fourier-filtered and 80% of the linear background is subtracted. The Gaussian (purple) and Lorentzian (rose) contributions to the spot intensity (corrected for instrumental resolution) are schematically depicted in logarithmic scale closely above T_c at $T = 198$ K in the right panel.

Below $T \approx 200$ K the spot profile of the $(3/4 \overline{1/2})$ spot consists of a sharp Gaussian contribution and a weaker Lorentzian part with constant intensity and FWHM. Both parts are schematically depicted in the right panel of Fig. 6 for $T = 198$ K and as \otimes and \oplus in Fig. 5(a), respectively. Above $T \approx 200$ K the central spike has disappeared, while the width of the broad diffuse part increases strongly. However, the diffuse part is still clearly visible at room temperature [see also the streaks of the LEED pattern in Fig. 4(a)] and above. In contrast, all integer order spots like the (00) spot and all half-integer order spots always exhibit a spot profile given solely by a sharp Gaussian with constant FWHM independent of temperature [cf. Fig. 5(d,e)].

The fits to the line profiles of the $(3/4 \overline{1/2})$ spot, namely the Debye-Waller-corrected intensities of the Gaussian central spike I_G and of the broad diffuse Lorentzian I_L , as well

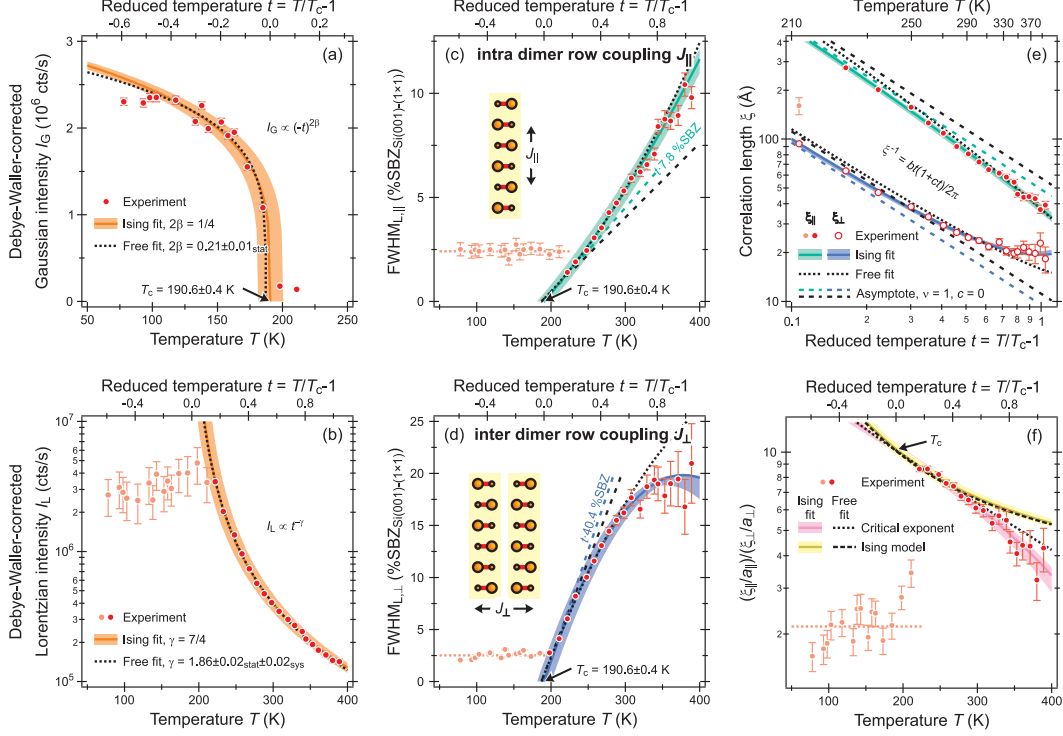


FIG. 7. Order-disorder phase transition in Si(001). Critical behavior of the Gaussian (a) and Lorentzian (b) contributions $I_{G,L}$ to the $(3/4 \ 1\bar{2})$ spot intensity during and above the phase transition, respectively. Data are corrected for the Debye-Waller effect. (c,d) Temperature-dependent FWHMs of the Lorentzian contribution to the $(3/4 \ 1\bar{2})$ spot profile along (along $[110]$ direction, intra dimer row coupling) and across (along $[1\bar{1}0]$ direction, inter dimer row coupling) the dimer rows corrected for the instrumental resolution, respectively. (e) Correlation lengths $\xi_{\parallel,\perp}$ of the Lorentzian contribution vs. reduced temperature t above T_c . (f) Correlation length ratio $(\xi_{\parallel}/a_{\parallel})/(\xi_{\perp}/a_{\perp})$ of the Lorentzian contribution. Data are fitted for (a) $T \in [95 \text{ K}, T_c)$, (b) $T \in [225 \text{ K}, 400 \text{ K}]$, (c) $T \in [220 \text{ K}, 300 \text{ K}]$ and (d) $T \in [210 \text{ K}, 300 \text{ K}]$. Light pink data points belong to the so-called domain state and are not taken into account for the fits in (b-f). Colored lines indicate fits to the critical behavior predicted by Onsager theory, determining the critical temperature $T_c = (190.6 \pm 0.4_{\text{stat}} \pm 9.6_{\text{sys}}) \text{ K}$. First order corrections are taken into account for the FWHMs and the correlation lengths in (c-e), respectively. The asymptotic (linear) behavior is shown by the colored dashed lines in (c-e). In (f) the expected behavior for the 2D Ising model (dark yellow line) is derived by matching the values with the results from the fit to the critical behavior (dark pink line) at T_c . The reduced temperature t is derived from Ising model $T_c = 190.6 \text{ K}$. Shaded areas indicate corresponding systematic errors, accordingly. Black dotted lines indicate fits to the critical behavior with unfixed exponents β and γ .

as both Lorentzian peak widths $\text{FWHM}_{\text{L},\delta}$ are further analyzed and compared with the theoretical predictions of the anisotropic 2D Ising model. Both intensity contributions vary strongly with temperature, i.e., reflecting the critical behavior of the phase transition. The critical temperature $T_c = (190.6 \pm 0.4_{\text{stat}} \pm 9.6_{\text{sys}})$ K is derived by a global fit of all four critical quantities for temperatures up to 310 K colored solid lines (shaded areas indicate systematic errors) in Fig. 7(a-d)], i.e., $I_{\text{G,L}}$ and $\text{FWHM}_{\text{L},\delta}$. The Gaussian contribution [Fig. 7(a)] exhibits a sharp drop around 200 K, indicative of the order-disorder phase transition [25, 33]. The orange solid line is a fit to the critical behavior following the power law $(-t)^{2\beta}$ proportional to the square of the order parameter Ψ with $\beta = 1/8$.

For $T > T_c$ the $(3/4 \sqrt{1/2})$ spot exhibits a Lorentzian profile with decreasing peak intensity [Fig. 7(b)] and increasing widths along both directions (cf. Fig. 6) as function of temperature. The orange solid line is a fit to the intensity above T_c , which is proportional to the susceptibility χ and scales with the power law $|t|^{-\gamma}$ with $\gamma = 7/4$.

The Lorentzian FWHMs along and across the dimer rows are shown in Fig. 7(c,d). Starting at T_c , both FWHMs increase asymptotically from zero (colored dashed lines) with $\text{FWHM}_{\text{L},\parallel}/t = b_{\parallel} = (7.8 \pm 0.3_{\text{stat}} \pm 1.0_{\text{sys}}) \% \text{SBZ}$ and $\text{FWHM}_{\text{L},\perp}/t = b_{\perp} = (40.4 \pm 0.8_{\text{stat}} \pm 5.0_{\text{sys}}) \% \text{SBZ}$, respectively. The fit (colored solid lines) to the data shows a deviation from the asymptotes, which is well described up to $T \approx 300$ K by a first-order correction term to the Lorentzian FWHMs, i.e., $\text{FWHM}_{\text{L},\delta}(t) = b_{\delta}t(1 + c_{\delta}t + \dots)$ for $T > T_c$ [81]. Approaching T_c , i.e., $t \rightarrow 0^+$, both correlation lengths $\xi_{\delta}(t) = 2\pi/\text{FWHM}_{\text{L},\delta}(t)$ diverge according to Eq. (7c) with an exponent $\nu = 1$ [colored dashed lines in Fig. 7(e)].

Comparing the experimentally observed temperature dependence of the Lorentzian correlation length ratio $(\xi_{\parallel}/a_{\parallel})/(\xi_{\perp}/a_{\perp})$ above T_c with the exact solution Eq. (8) of the 2D Ising model [see Fig. 7(f)] we derive by extrapolation $t \rightarrow 0^+$

$$\lim_{t \rightarrow 0^+} \frac{\xi_{\parallel}(t)/a_{\parallel}}{\xi_{\perp}(t)/a_{\perp}} = \frac{a_{\perp}b_{\perp}}{a_{\parallel}b_{\parallel}} = 10.29 \pm 0.39_{\text{stat}} \pm 0.01_{\text{sys}}. \quad (14)$$

Using Eq. (10) at T_c , we finally derive the coupling energies as $J_{\parallel} = (-24.9 \pm 0.9_{\text{stat}} \pm 1.3_{\text{sys}})$ meV and $J_{\perp} = (-0.8 \pm 0.1_{\text{stat}})$ meV. The negative sign of both couplings follows from the spot positions in the diffraction pattern, leading to an antiferromagneticlike coupling of the dimers along and across the dimer rows with $c(4 \times 2)$ symmetry. Eventually, we obtain the coupling energy ratio $J_{\parallel}/J_{\perp} = 31.2 \pm 3.8_{\text{stat}}$.

In addition to the analysis within the anisotropic 2D Ising model, we fitted the critical

TABLE IV. **Critical behavior of the $(3/4\ 1/2)$ spot.** Fit results including statistical (stat, first) and systematic (sys, second) errors.

	Ising model fit	Free fit
T_c (K)	$190.6 \pm 0.4 \pm 9.6$	$187.1 \pm 0.6 \pm 9.0$
2β	0.25	$0.21 \pm 0.01 \pm 0$
γ	1.75	$1.86 \pm 0.02 \pm 0.02$
b_{\parallel} (%SBZ)	$7.8 \pm 0.3 \pm 1.0$	$6.7 \pm 0.3 \pm 0.3$
c_{\parallel}	$0.32 \pm 0.09 \pm 0.29$	$0.56 \pm 0.10 \pm 0.09$
J_{\parallel} (meV)	$-24.9 \pm 0.9 \pm 1.3$	$-24.4 \pm 1.2 \pm 1.2$
b_{\perp} (%SBZ)	$40.4 \pm 0.8 \pm 5.0$	$34.5 \pm 1.0 \pm 1.5$
c_{\perp}	$-0.51 \pm 0.04 \pm 0.22$	$-0.29 \pm 0.05 \pm 0.06$
J_{\perp} (meV)	$-0.8 \pm 0.1 \pm 0$	$-0.8 \pm 0.1 \pm 0$
b_{\perp}/b_{\parallel}	$5.15 \pm 0.20 \pm 0$	$5.16 \pm 0.25 \pm 0$
J_{\parallel}/J_{\perp}	$31.2 \pm 3.8 \pm 0$	$31.3 \pm 4.9 \pm 0$

behavior of the system with free exponents 2β and γ . With this method we can determine how well the Si dimers behave as expected for an Ising system or another universality class. The results of the global fit are shown in Fig. 7 as black dotted lines. For comparison, the results of both fits, i.e., for free exponents and for the anisotropic 2D Ising model with $2\beta = 1/4$ and $\gamma = 7/4$ are summarized in Table IV. As we find for the free fit $T_c = (187.1 \pm 0.5_{\text{stat}} \pm 9.0_{\text{sys}})$ K, $2\beta = 0.21 \pm 0.01_{\text{stat}}$ and $\gamma = 1.86 \pm 0.02_{\text{stat}} \pm 0.02_{\text{sys}}$, we can confirm that the system behaves Ising-like. For the free fit the coupling constants are derived as $J_{\parallel} = (-24.4 \pm 1.2_{\text{stat}} \pm 1.2_{\text{sys}})$ meV and $J_{\perp} = (-0.8 \pm 0.1_{\text{stat}})$ meV, and thus $J_{\parallel}/J_{\perp} = 31.3 \pm 4.9_{\text{stat}}$, very close to the results of the anisotropic 2D Ising model.

The large deviation of the Lorentzian intensity, FWHMs and correlation length ratio for $T \leq T_c$ (light pink data points in Fig. 7) from the expected behavior of the 2D Ising model is due to the formation of finite-sized ordered domains. The fluctuating dimer system was quenched upon passing the critical temperature during cooling, i.e., reflecting the frozen critical fluctuations at $T > T_c$. Here, we observe constant and isotropic Lorentzian FWHMs $\text{FWHM}_{L,\perp} = (2.52 \pm 0.01_{\text{stat}})$ %SBZ and $\text{FWHM}_{L,\parallel} = (2.41 \pm 0.07_{\text{stat}})$ %SBZ, respectively, i.e., the resulting domain size is limited by the quench to about 14 nm.

Finally, we analyze the Lorentz scaling function $A_L^+(y_\delta^+)$ above T_c from Eq. (13c), with direction $\delta \in \{\parallel, \perp\}$ and scaling variable y_δ^+ from Eq. (13d). For this, in Fig. 8 we plot the Debye-Waller-corrected experimental data for temperatures $222 \text{ K} \leq T \leq 320 \text{ K}$ as a scaling plot, by rescaling the abscissa $q_\delta - q_{0,\delta}$ with the correlation length $\xi_\delta(t)$ from Eq. (7c) and the ordinate $I_L(q_\delta, t)$ with the inverse susceptibility $\chi(t)^{-1}$ from Eq. (7b). We obtain an impressive quantitative data collapse of the different intensities in both directions without applying any further fitting parameters. The systematic deviations at negative y_\perp^+ are due to the enhanced intensity at $q_\perp = 50 \text{ \%SBZ}$ originating from the neighboring quarter-integer order spots (cf. left panel of Fig. 6). The data fall nicely onto the Ornstein-Zernike prediction $A_{OZ}(y) = (1 + y^2)^{-1}$ (black solid curve). We also show the exact scaling function obtained by Tracy and McCoy [86, Eq. (B7)] (red dashed curve), which is barely distinguishable from $A_{OZ}(y)$ at these small values of $|y_\delta^+|$.

VI. DISCUSSION & CONCLUSIONS

Comparing the interaction parameters derived from the electron diffraction experiment via fitting to the Ising model, $J_\parallel = (-24.9 \pm 0.9_{\text{stat}} \pm 1.5_{\text{sys}}) \text{ meV}$ and $J_\perp = (-0.8 \pm 0.1_{\text{stat}} \pm 0.2_{\text{sys}}) \text{ meV}$ with $T_c = (190.6 \pm 0.4_{\text{stat}} \pm 9.6_{\text{sys}}) \text{ K}$ with the values calculated from DFT (Table II), we conclude that all the three considered functionals predict the critical temperature in the correct range, between 190 K and 214 K, with the PBEsol functional coming closest to the experimental value of T_c . However, the anisotropy ratio J_\parallel/J_\perp varies strongly, between 15.7 for the LDA and 63.1 for the PBE functional. Again, the PBEsol functional, which yields an anisotropy ratio of 40, comes closest to the experimental value of $31.2 \pm 3.8_{\text{stat}}$ in the Ising model fit ($31.3 \pm 4.9_{\text{stat}}$ in the free fit). This demonstrates a compensation effect: a functional that overestimates J_\parallel tends to underestimate J_\perp and vice versa. Since these two interactions enter in opposite ways into Eq. (6) for T_c , the predicted value of T_c is quite robust. Only with the help of subtle experimental methods, i.e., the spot profile analysis of diffraction spots, has the anisotropy parameter become experimentally accessible, allowing us to evaluate the performance of the different DFT functionals. We find that the PBEsol functional, whose construction was motivated by improving the values of surface energies, also performs best in predicting the critical behavior of the order-disorder phase transition. We trace back this excellent performance of the PBEsol functional to yielding the correct

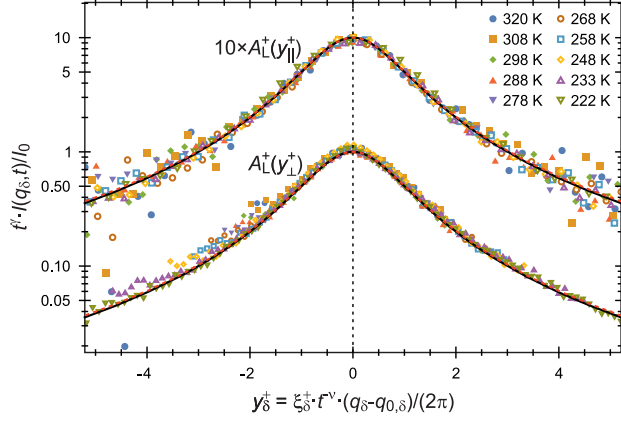


FIG. 8. Scaling plot of the Lorentz scaling function $A_L^+(y_\delta^+)$ above T_c from Eq. (13c), with direction $\delta \in \{\parallel, \perp\}$ and scaling variable y_δ^+ from Eq. (13d). The black solid line is the Ornstein-Zernike prediction $A_{OZ}(y) = (1 + y^2)^{-1}$, while the red dashed line is the exact Ising scaling function from Ref. 86, Eq. (B7).

lattice constant and the surface stress anisotropy associated with the Si(001) surface reconstruction. The PBEsol results, yielding $J_\parallel = -27.1$ meV, $J_\perp = -0.7$ meV and $T_c = 195.9$ K, are strikingly close to the experiment.

Discrepancies between the experimental results and earlier theoretical predictions of T_c have been interpreted as a result of overestimated defect concentrations in the percent range within the dimer structure [35, 87–92]. We have shown in this study that such an explanation is incorrect for clean surfaces with low defect concentrations. The critical temperature of $T_c = 190.6$ K is a robust result because it is directly related to the interaction energies of the dimers via Eq. (6).

The very small value of J_\perp and the pertinent small energy difference between the $c(4 \times 2)$ and $p(2 \times 2)$ structure are also consistent with the coexistence of $c(4 \times 2)$ and $p(2 \times 2)$ domains sometimes observed in STM images at low temperatures [93]. Even slight perturbations of the surface by the electric field and/or the current generated by the STM tip may be sufficient to switch between the two reconstructions. In addition, low-temperature STM experiments at elevated tip voltage show dynamic changes of the Si dimer buckling [52, 60], in particular at the boundary between the $c(4 \times 2)$ and $p(2 \times 2)$ domains. The (mobile) surface excitations observed in such an experiment are called phasons [93], where a phason (or antiphason) corresponds to two adjacent Si dimers tilted in the same direction in an otherwise completely

ordered environment. Phasons can move along a Si dimer row and can only be created or annihilated as phason-antiphason pairs. In this sense, they are topological defects in an ordered 1D structure. A Si dimer chain bounded by a phason and an antiphason can be viewed as a domain whose order is out-of-phase with the surrounding $c(4\times 2)$ structure. The finite length of such a dimer chain leads to a broadening of the $(3/4\ \overline{1/2})$ diffraction spot in a LEED image. Therefore the Lorentzian FWHM of this quarter-integer order LEED spot is a measure of the phason density. Thus, the size of ordered domains is determined by a geometric length distribution [94], i.e., the correlations decay on large length scales r for $T > T_c$ as $\propto \exp(-r/\xi_\delta)$ [40].

VII. SUMMARY & OUTLOOK

Our comprehensive DFT and SPA-LEED results paint a new picture for the microscopic understanding of second-order phase transitions on surfaces. The dimerized Si(001) surface is a prototypical system that exhibits such a phase transition at a critical temperature of $T_c = 190.6$ K. Due to the dimerization of the topmost surface layer on the square bulk-terminated Si(001) face, the dimers are arranged in dimer rows and thus anisotropic coupling between the dimers is observed. Mapping of the anisotropic 2D Ising model for spins on a rectangular lattice onto the structure of Si dimers allows for a quantitative theoretical description of the experimentally observed phase transition. The microscopic details of the (electrostatic) coupling between the individual dimers described by the Ising model determine the critical temperature of the order-disorder phase transition. Our DFT calculations go a step beyond the simple anisotropic 2D Ising model by considering longer-ranging interactions. At the same time, the effective lattice Hamiltonian derived from our DFT results yields the same critical behavior as the anisotropic 2D Ising model.

The understanding of the order-disorder phase transition gained in the framework of the anisotropic 2D Ising model allows us to analyze non-equilibrium states of the Si(001) surface that could be obtained, e.g., by rapid cooling of the surface below T_c . If the cooling is sufficiently fast, different domains of the $c(4\times 2)$ structure, bounded by a phason and antiphason, could be frozen in, analogous to the kinetically limited domain structure already observed in our experiments, as reported in Sec. V. This could be the subject of future research, e.g. in experiments where the cooling rate is systematically varied over a wide

range.

From the theoretical perspective, general considerations concerning the creation and persistence of defects while swiftly crossing a phase transition can be helpful in making predictions about the domain structure. The density of phasons and antiphasons can only be reduced, i.e., a perfectly ordered surface can only be achieved, if these defects have sufficient time to propagate, meet and annihilate. Thus, small domains can be eliminated during cooling, while larger ones will persist even below T_c . Given that the Kibble-Zurek mechanism [95, 96] applies, a scaling law is predicted: the initial size of the domains that persist during cooling scales like $(\tau_Q/\tau_0)^\alpha$, where τ_Q is the time scale associated with cooling, defined by $t/\tau_Q = 1 - T(t)/T_c$, and τ_0 is an intrinsic time scale of the system, here associated with the flipping rate of the Si dimers. The exponent $\alpha \approx 0.3$ is related to the dynamic scaling exponent z of the underlying 2D Ising model. Thus, studying the Si(001) surface under non-equilibrium conditions in combination with a scaling analysis could provide valuable information about the microscopic time scale associated with Si dimer flipping.

APPENDIX: Comparison to prior lattice Hamiltonians

In early works [35, 70, 71], researchers included in their Hamiltonians three interactions C_V , C_H and C_D , along, across, and diagonal to the Si dimer rows (cf. Table V). Later, conditional longer-ranged interactions (C_{V3} and C_{V4}) were added [47, 72], which contribute only when three or four adjacent dimers are tilted in the same direction. In this work, we explore two approaches, simply adding C_{V3} or adding both C_{V3} and C_{V4} . To retain consistency with the literature on spin models, we prefer an equivalent representation of the Hamiltonians in terms of (unconditional) NNN interactions C_{V3} and quadruple interactions C_{V4} . Thus, the generalized Ising model Hamiltonians used to fit our DFT results read

$$\begin{aligned} \mathcal{H}_0 &= -C_V \sum_{i,j} \sigma_{i,j} \sigma_{i,j+1} - C_H \sum_{i,j} \sigma_{i,j} \sigma_{i+1,j} - C_D \sum_{i,j} \sigma_{i,j} (\sigma_{i+1,j+1} + \sigma_{i+1,j-1}) \\ &\quad - C_{V3} \sum_{i,j} (1 + \sigma_{i,j} \sigma_{i,j-1} + \sigma_{i,j} \sigma_{i,j+1} + \sigma_{i,j-1} \sigma_{i,j+1}) , \\ \mathcal{H}_1 &= \mathcal{H}_0 - C_{V4} \sum_{i,j} (1 + \sigma_{i,j} \sigma_{i,j-1} + \sigma_{i,j} \sigma_{i,j+1} + \sigma_{i,j} \sigma_{i,j+2} + \sigma_{i,j-1} \sigma_{i,j+1} + \sigma_{i,j-1} \sigma_{i,j+2} + \sigma_{i,j+1} \sigma_{i,j+2} \\ &\quad + \sigma_{i,j} \sigma_{i,j-1} \sigma_{i,j+1} \sigma_{i,j+2}) . \end{aligned} \tag{A.1}$$

The coupling parameters of the lattice Hamiltonians given in Eqs. (A.1) and (A.2) are determined by solving a system of linear equations corresponding to the tilting patterns considered in Fig. 2:

$$E_{c(4 \times 2)} = E_0 + 12 [C_V + (C_H - 2C_D)] , \quad (\text{A.3a})$$

$$E_{p(2 \times 2)} = E_0 + 12 [C_V - (C_H - 2C_D)] , \quad (\text{A.3b})$$

$$E_{\text{SDF}} = E_0 + 8 [C_V + (C_H - 2C_D)] - 4C_{V3} , \quad (\text{A.3c})$$

$$E_{\text{TDF}} = E_0 + 4 [2C_V + (C_H - 2C_D)] , \quad (\text{A.3d})$$

$$E_{\text{SDF-2R}} = E_0 + 4 [C_V + 2C_H + (C_H - 2C_D)] - 8C_{V3} , \quad (\text{A.3e})$$

$$E_{p(4 \times 1)} = E_0 - 12 (C_V - 2C_H + (C_H - 2C_D) + 4C_{V3} + 8C_{V4}) , \quad (\text{A.3f})$$

$$E_{p(2 \times 1)} = E_0 - 12 (C_V + 2C_H - (C_H - 2C_D) + 4C_{V3} + 8C_{V4}) . \quad (\text{A.3g})$$

The quantities on the left sides are the DFT total energies of the dimer tilting patterns in the (6×4) supercell and E_0 is a constant accounting for the contribution into the total energy from the Si structure underneath the top-most dimerized atomic layer. To determine the interaction parameters of \mathcal{H}_0 we considered only the five energetically lowest structures (cf. Tab. I), Eqs. (A.3a) to (A.3e).

For comparison with previous literature (cf. Table V), we have also parameterized a Hamiltonian \mathcal{H}_1 [Eq. (A.2)] and included the resulting interaction parameters in Table VI. The equated results to \mathcal{H}_1 are based on all equations except Eq. (A.3e), as this was the previously used set of patterns. With the exception of the early results of Inoue *et al.* [35] who obtained an unusually large value of C_V , the results are in reasonable agreement with each other. In particular, the tight-binding (TB) calculations also describe the leading interaction term C_V with the correct magnitude. However, neglecting both C_{V3} and C_{V4} (cf. Refs. 35 and 70) leads to an overestimation of the remaining coupling parameters.

It should be noted that the selection of tilting patterns for the computation of the interaction energies of the Hamiltonian \mathcal{H}_0 (cf. Table VI), in particular the $p(2 \times 1)$ and $p(4 \times 1)$ structures, leads to much larger values of C_H and C_D compared to the Hamiltonian \mathcal{H}_0 . However, these two interactions of opposite sign largely cancel out when the effective interaction J_\perp is calculated. Moreover, the inclusion of the energetically high-lying $p(2 \times 1)$

TABLE V. **Comparison to previous results.** Interaction energies are given in meV. T_c is derived by Eq. (6) using the values of J_δ . Energies C_{V3} and C_{V4} from literature are converted to our re-definition according to Eqs. (A.1) and (A.2). The * indicates a phase transition from the disordered $p(2\times 1)$ phase to the $p(2\times 2)$ phase as ground state instead of the $c(4\times 2)$ phase. Note that Xiao *et al.* [72], when quoting their numbers for C_H and C_D in their Table II, forgot to divide by a factor of 2. This must be concluded from their total energies in Table I that are used as input to determine C_H and C_D . Also their C_{V4} was miscalculated.

	LDA		PBE	PW91	TB	
	Inoue	Pillay	Xiao	Pillay	Ihm	Fu
	[35]	[47]	[72]	[47]	[70]	[97]
$C_V = J_\parallel$	-51.9	-16.8	-37.4	-25.3	-26.0	-32.4
C_H	6.6	6.4	7.9	7.5	10.0	0.6
C_D	3.6	4.2	4.0	4.1	4.0	0.6
C_{V3}	-	0.1	-3.7	-4.2	-	-2.7
C_{V4}	-	-5.3	-1.9	-2.7	-	-
$J_\perp = C_H - 2C_D$	-0.6	-2.0	-0.1	-0.7	2.0	-0.6
J_\parallel/J_\perp	86.5	8.4	374.0	36.7	-13.0*	54.0
T_c (K)	315.8	186.6	173.4	187.1	252.5	218.3

structure in the calculation forces an unphysically large value of C_{V4} . To date, neither the $p(2\times 1)$ nor the $p(4\times 1)$ structure have been observed experimentally as long-range ordered reconstructions. This is consistent with our finding that both patterns are thermodynamically unfavorable by $\approx 0.85 - 1.3$ eV compared to the other five patterns considered over all exchange-correlation functionals used in the present work. In contrast, the four interaction energies C_V , C_H , C_D , and C_{V3} are determined using the five most stable tilting patterns. Thus, we consider the Hamiltonian \mathcal{H}_0 with four interaction terms to be physically more realistic, and thus better describing the underlying physics of the Si(001) surface than the Hamiltonian \mathcal{H}_1 with five interaction terms. In fact, as we showed in Sec. III C, even two *effective* interaction parameters, J_\parallel and J_\perp , are sufficient to describe the critical behavior close to the order-disorder phase transition.

TABLE VI. **DFT results on interaction energies II.** Interaction energies are given in meV. T_c is derived by Eq. (6) using the values of J_δ .

	LDA		PBE		PBEsol	
$C_V = J_\parallel$	-22.6	-22.6	-29.4	-29.4	-26.1	-26.1
C_H	3.9	5.7	5.5	7.0	3.4	6.5
C_D	2.7	3.6	3.0	3.8	2.0	3.6
C_{V3}	-2.2	-2.2	-2.4	-2.4	-1.1	-1.1
C_{V4}	-	-3.6	-	-2.9	-	-3.9
$J_\perp = C_H - 2C_D$	-1.6	-1.6	-0.5	-0.5	-0.7	-0.7
J_\parallel/J_\perp	14.3	14.3	56.5	56.5	38.5	38.5
T_c (K)	213.7	213.8	196.2	196.2	190.1	190.1
a_{lat} (Å)	5.38		5.46		5.43	

AUTHOR CONTRIBUTIONS

G.J., and R.H. performed the experiments. C.B., and A.H. analyzed the data and prepared the figures. H.M. performed DFT calculations. C.B., H.M., A.H., P.K., and M.H.-v.H. drafted the manuscript. M.H.-v.H., A.H., B.S., P.K., and R.S. conceived and supervised the project. The manuscript was written through contributions of all authors. All authors have given approval to the final version of the manuscript.

The authors declare no competing financial interest.

ACKNOWLEDGEMENTS

Funded by the Deutsche Forschungsgemeinschaft (DFG, German Research Foundation) through projects A02, B02, B03, B07, and C03 of Collaborative Research Center SFB1242 “Nonequilibrium dynamics of condensed matter in the time domain” (Project-ID 278162697).

-
- [1] J. R. Ahn, J. H. Byun, H. Koh, E. Rotenberg, S. D. Kevan, and H. W. Yeom, Mechanism of gap opening in a triple-band Peierls system: In atomic wires on Si, *Phys. Rev. Lett.* **93**,

- 106401 (2004).
- [2] C. Kumpf, O. Bunk, J. H. Zeysing, Y. Su, M. Nielsen, R. L. Johnson, R. Feidenhans'l, and K. Bechgaard, Low-Temperature Structure of Indium Quantum Chains on Silicon, *Phys. Rev. Lett.* **85**, 4916 (2000).
 - [3] S. Wippermann and W. G. Schmidt, Entropy Explains Metal-Insulator Transition of the Si(111)-In Nanowire Array, *Phys. Rev. Lett.* **105**, 126102 (2010).
 - [4] W. G. Schmidt, S. Wippermann, S. Sanna, M. Babilon, N. J. Vollmers, and U. Gerstmann, In-Si(111)(4×1)/(8×2) nanowires: Electron transport, entropy, and metal-insulator transition, *Phys. Status Solidi B* **249**, 343 (2012).
 - [5] S. C. Erwin and F. J. Himpsel, Intrinsic magnetism at silicon surfaces, *Nat. Commun.* **1**, 1 (2010).
 - [6] B. Hafke, C. Brand, T. Witte, B. Sothmann, M. Horn-von Hoegen, and S. C. Erwin, Thermally Induced Crossover from 2D to 1D Behavior in an Array of Atomic Wires: Silicon Dangling-Bond Solitons in Si(553)-Au, *Phys. Rev. Lett.* **124**, 016102 (2020).
 - [7] Z. Mamiyev, C. Fink, K. Holtgrewe, H. Pfnür, and S. Sanna, Enforced Long-Range Order in 1D Wires by Coupling to Higher Dimensions, *Phys. Rev. Lett.* **126**, 106101 (2021).
 - [8] P. C. Snijders and H. H. Weitering, Colloquium: Electronic instabilities in self-assembled atom wires, *Rev. Mod. Phys.* **82**, 307 (2010).
 - [9] M. Czubanowski, A. Schuster, S. Akbari, H. Pfnür, and C. Tegenkamp, Adsorbate induced refacetting: Pb chains on Si(557), *New J. Phys.* **9**, 338 (2007).
 - [10] H. Pfnür, C. Brand, M. Jäger, J. Rönspies, and C. Tegenkamp, Between one and two dimensions: Pb/Si(557) close to monolayer coverage, *Surf. Sci.* **643**, 79 (2016).
 - [11] C. Tegenkamp, D. Lükermann, H. Pfnür, B. Slomski, G. Landolt, and J. H. Dil, Fermi Nesting between Atomic Wires with Strong Spin-Orbit Coupling, *Phys. Rev. Lett.* **109**, 266401 (2012).
 - [12] C. Brand, H. Pfnür, G. Landolt, S. Muff, J. H. Dil, T. Das, and C. Tegenkamp, Observation of correlated spin-orbit order in a strongly anisotropic quantum wire system, *Nat. Commun.* **6**, 8118 (2015).
 - [13] L. Zhang, P. Bampoulis, A. Safaei, H. J. W. Zandvliet, and A. van Houselt, Structural and electronic properties of Pt induced nanowires on Ge(110), *Appl. Surf. Sci.* **387**, 766 (2016).
 - [14] H. W. Yeom, S. Takeda, E. Rotenberg, I. Matsuda, K. Horikoshi, J. Schaefer, C. M. Lee, S. D. Kevan, T. Ohta, T. Nagao, and S. Hasegawa, Instability and Charge Density Wave of Metallic

- Quantum Chains on a Silicon Surface, *Phys. Rev. Lett.* **82**, 4898 (1999).
- [15] T. Frigge, B. Hafke, T. Witte, B. Krenzer, C. Streubühr, A. S. Syed, V. M. Trontl, I. Avigo, P. Zhou, M. Ligges, *et al.*, Optically excited structural transition in atomic wires on surfaces at the quantum limit, *Nature* **544**, 207 (2017).
 - [16] J. Dąbrowski and H.-J. Müssig, *Silicon surfaces and formation of interfaces: basic science in the industrial world* (2000).
 - [17] H. E. Farnsworth, R. E. Schlier, T. H. George, and R. M. Burger, Application of the Ion Bombardment Cleaning Method to Titanium, Germanium, Silicon, and Nickel as Determined by Low-Energy Electron Diffraction, *J. Appl. Phys.* **29**, 1150 (1958).
 - [18] X.-Y. Ren, H.-J. Kim, C.-Y. Niu, Y. Jia, and J.-H. Cho, Origin of symmetric dimer images of Si(001) observed by low-temperature scanning tunneling microscopy, *Sci. Rep.* **6**, 1 (2016).
 - [19] R. E. Schlier and H. E. Farnsworth, Structure and adsorption characteristics of clean surfaces of germanium and silicon, *J. Chem. Phys.* **30**, 917 (1959).
 - [20] D. J. Chadi, Atomic and Electronic Structures of Reconstructed Si(100) Surfaces, *Phys. Rev. Lett.* **43**, 43 (1979).
 - [21] R. M. Tromp, R. J. Hamers, and J. E. Demuth, Si(001) Dimer Structure Observed with Scanning Tunneling Microscopy, *Phys. Rev. Lett.* **55**, 1303 (1985).
 - [22] P. C. Weakliem, G. W. Smith, and E. A. Carter, Subpicosecond interconversion of buckled and symmetric dimers on Si(100), *Surf. Sci.* **232**, L219 (1990).
 - [23] R. A. Wolkow, Direct observation of an increase in buckled dimers on Si(001) at low temperature, *Phys. Rev. Lett.* **68**, 2636 (1992).
 - [24] R. G. Zhao and W. S. Yang, Atomic structure of the Si(001) $c(4 \times 2)$ surface, *Phys. Rev. B* **33**, 6780 (1986).
 - [25] T. Tabata, T. Aruga, and Y. Murata, Order-disorder transition on Si(001): $c(4 \times 2)$ to (2×1) , *Surf. Sci.* **179**, L63 (1987).
 - [26] H. J. W. Zandvliet, The Ge(001) surface, *Phys. Rep.* **388**, 1 (2003).
 - [27] H. J. W. Zandvliet, W. J. Caspers, and A. van Silfhout, Order-disorder phase transition of the Ge(001) surface, *Solid State Commun.* **78**, 455 (1991).
 - [28] H. J. W. Zandvliet, D. Terpstra, and A. van Silfhout, Reconstructions and phase transitions of the Ge(001) surface, *J. Phys. Condens. Matter* **3**, 409 (1991).

- [29] C. A. Lucas, C. S. Dower, D. F. McMorro, G. C. L. Wong, F. J. Lamelas, and P. H. Fuoss, Order-disorder $c(4 \times 2) - (2 \times 1)$ transition on Ge(001): An in situ x-ray scattering study, *Phys. Rev. B* **47**, 10375 (1993).
- [30] D. Cvetko, L. Floreano, A. Crottini, A. Morgante, and F. Tommasini, Disordering of the Ge(001) surface studied by He atom scattering, *Surf. Sci.* **447**, L147 (2000).
- [31] S. D. Kevan, Surface states and reconstruction on Ge(001), *Phys. Rev. B* **32**, 2344 (1985).
- [32] M. Kubota and Y. Murata, Streak patterns in low-energy electron diffraction on Si(001), *Phys. Rev. B* **49**, 4810 (1994).
- [33] Y. Murata and M. Kubota, Order-disorder transition on Si(001), *Phase Transit.* **53**, 125 (1995).
- [34] M. Matsumoto, K. Fukutani, and T. Okano, Low-Energy Electron Diffraction Study of the Phase Transition of Si(001) Surface below 40 K, *Phys. Rev. Lett.* **90**, 106103 (2003).
- [35] K. Inoue, Y. Morikawa, K. Terakura, and M. Nakayama, Order-disorder phase transition on the Si(001) surface: Critical role of dimer defects, *Phys. Rev. B* **49**, 14774 (1994).
- [36] C. Brand, A. Hucht, G. Jnawali, J. D. Fortmann, B. Sothmann, H. Mehdipour, P. Kratzer, R. Schützhold, and M. Horn-von Hoegen, Dimer Coupling Energies of the Si(001) Surface, *Phys. Rev. Lett.* **130**, 126203 (2023).
- [37] L. P. Kadanoff, Scaling laws for Ising models near T_c , *Physics Physique Fizika* **2**, 263 (1966).
- [38] M. E. Fisher, Renormalization group theory: Its basis and formulation in statistical physics, *Rev. Mod. Phys.* **70**, 653 (1998).
- [39] L. Onsager, Crystal Statistics. I. A Two-Dimensional Model with an Order-Disorder Transition, *Phys. Rev.* **65**, 117 (1944).
- [40] B. M. McCoy and T. T. Wu, *The Two-Dimensional Ising Model* (Harvard University Press, 2013).
- [41] A. Ramstad, G. Brocks, and P. J. Kelly, Theoretical study of the Si(100) surface reconstruction, *Phys. Rev. B* **51**, 14504 (1995).
- [42] K. Wandelt, *Surface and Interface Science. Volume 2: Properties of Elemental Surfaces* (Wiley Online Library, 2012).
- [43] Y. Fukaya and Y. Shigeta, Phase transition from asymmetric to symmetric dimer structure on the Si(001) surface at high temperature, *Phys. Rev. Lett.* **91**, 126103 (2003).
- [44] H. Over, J. Wasserfall, W. Ranke, C. Ambiatello, R. Sawitzki, D. Wolf, and W. Moritz, Surface atomic geometry of Si(001)-(2 \times 1): A low-energy electron-diffraction structure analysis, *Phys.*

- Rev. B **55**, 4731 (1997).
- [45] R. Felici, I. K. Robinson, C. Ottaviani, P. Imperatori, P. Eng, and P. Perfetti, Room temperature Si(001)-(2 \times 1) reconstruction solved by X-ray diffraction, *Surf. Sci.* **375**, 55 (1997).
 - [46] T. Shirasawa, S. Mizuno, and H. Tochiara, Structural analysis of the c(4 \times 2) reconstruction in Si(001) and Ge(001) surfaces by low-energy electron diffraction, *Surf. Sci.* **600**, 815 (2006).
 - [47] D. Pillay, B. Stewart, C. B. Shin, and G. S. Hwang, Revisit to the Ising model for order–disorder phase transition on Si(001), *Surf. Sci.* **554**, 150 (2004).
 - [48] C.-S. Guo, K. Hermann, and Y. Zhao, Dynamics and Energetics of Reconstruction at the Si(100) Surface, *J. Phys. Chem. C* **118**, 25614 (2014).
 - [49] J. Dąbrowski and M. Scheffler, Self-consistent study of the electronic and structural properties of the clean Si(001)(2 \times 1) surface, *Appl. Surf. Sci.* **56–58**, 15 (1992).
 - [50] E. Landemark, C. J. Karlsson, Y.-C. Chao, and R. I. G. Uhrberg, Core-level spectroscopy of the clean Si(001) surface: Charge transfer within asymmetric dimers of the 2 \times 1 and c(4 \times 2) reconstructions, *Phys. Rev. Lett.* **69**, 1588 (1992).
 - [51] S. Yoshida, T. Kimura, O. Takeuchi, K. Hata, H. Oigawa, T. Nagamura, H. Sakama, and H. Shigekawa, Probe effect in scanning tunneling microscopy on Si(001) low-temperature phases, *Phys. Rev. B* **70**, 235411 (2004).
 - [52] Y. Pennec, M. Horn-von Hoegen, X. Zhu, D. C. Fortin, and M. R. Freeman, Dynamics of an Ising Chain under Local Excitation: A Scanning Tunneling Microscopy Study of Si(100) Dimer Rows at 5 K, *Phys. Rev. Lett.* **96**, 026102 (2006).
 - [53] H. Shigekawa, K. Miyake, M. Ishida, K. Hata, H. Oigawa, Y. Nannichi, R. Y. Ozawa, and T. Nagamura, Phase Transition between c(4 \times 2) and p(2 \times 2) Structures of the Si(100) Surface at 6 K Caused by the Fluctuation of Phase Defects on Dimer Rows due to Dimer Flip-Flop Motion, *Jpn. J. Appl. Phys.* **35**, L1081 (1996).
 - [54] T. Yokoyama and K. Takayanagi, Anomalous flipping motions of buckled dimers on the Si(001) surface at 5 K, *Phys. Rev. B* **61**, R5078 (2000).
 - [55] K. Hata, S. Yoshida, and H. Shigekawa, p(2 \times 2) Phase of Buckled Dimers of Si(100) Observed on *n*-Type Substrates below 40 K by Scanning Tunneling Microscopy, *Phys. Rev. Lett.* **89**, 286104 (2002).
 - [56] T. Shirasawa, S. Mizuno, and H. Tochiara, Electron-Beam-Induced Disordering of the Si(001)-c(4 \times 2) Surface Structure, *Phys. Rev. Lett.* **94**, 195502 (2005).

- [57] S. Mizuno, T. Shirasawa, Y. Shiraishi, and H. Tochiyama, Structure determination of Si(001)- $c(4 \times 2)$ surfaces at 80 K and electron beam effect below 40 K studied by low-energy electron diffraction, *Phys. Rev. B* **69**, 241306 (2004).
- [58] K. Seino, W. G. Schmidt, and F. Bechstedt, Energetics of Si(001) Surfaces Exposed to Electric Fields and Charge Injection, *Phys. Rev. Lett.* **93**, 036101 (2004).
- [59] H. Kawai, O. Narikiyo, and K. Matsufuji, Structural Phase Transition between $c(4 \times 2)$ and $p(2 \times 2)$ Structures on Si(001) Surface under Observation by Scanning Tunneling Microscopy, *J. Phys. Soc. Jpn.* **76**, 034602 (2007).
- [60] K. Sagisaka, D. Fujita, and G. Kido, Phase Manipulation between $c(4 \times 2)$ and $p(2 \times 2)$ on the Si(100) Surface at 4.2 K, *Phys. Rev. Lett.* **91**, 146103 (2003).
- [61] K. Sagisaka and D. Fujita, Emergence of $p(2 \times 2)$ on highly doped n -type Si(100) surfaces: A scanning tunneling microscopy and spectroscopy study, *Phys. Rev. B* **71**, 245319 (2005).
- [62] S. B. Healy, C. Filippi, P. Kratzer, E. Penev, and M. Scheffler, Role of Electronic Correlation in the Si(100) Reconstruction: A Quantum Monte Carlo Study, *Phys. Rev. Lett.* **87**, 016105 (2001).
- [63] P. Giannozzi, S. Baroni, N. Bonini, M. Calandra, R. Car, C. Cavazzoni, D. Ceresoli, G. L. Chiarotti, M. Cococcioni, I. Dabo, A. D. Corso, S. de Gironcoli, S. Fabris, G. Fratesi, R. Gebauer, U. Gerstmann, C. Gougoussis, A. Kokalj, M. Lazzeri, L. Martin-Samos, N. Marzari, F. Mauri, R. Mazzarello, S. Paolini, A. Pasquarello, L. Paulatto, C. Sbraccia, S. Scandolo, G. Sclauzero, A. P. Seitsonen, A. Smogunov, P. Umari, and R. M. Wentzcovitch, QUANTUM ESPRESSO: a modular and open-source software project for quantum simulations of materials, *J. Phys. Condens. Matter* **21**, 395502 (2009).
- [64] J. P. Perdew and A. Zunger, Self-interaction correction to density-functional approximations for many-electron systems, *Phys. Rev. B* **23**, 5048 (1981).
- [65] J. P. Perdew, K. Burke, and M. Ernzerhof, Generalized Gradient Approximation Made Simple, *Phys. Rev. Lett.* **77**, 3865 (1996).
- [66] J. P. Perdew, A. Ruzsinszky, G. I. Csonka, O. A. Vydrov, G. E. Scuseria, L. A. Constantin, X. Zhou, and K. Burke, Restoring the Density-Gradient Expansion for Exchange in Solids and Surfaces, *Phys. Rev. Lett.* **100**, 136406 (2008).
- [67] C. Hartwigsen, S. Goedecker, and J. Hutter, Relativistic separable dual-space Gaussian pseudopotentials from H to Rn, *Phys. Rev. B* **58**, 3641 (1998).

- [68] D. Vanderbilt, Soft self-consistent pseudopotentials in a generalized eigenvalue formalism, *Phys. Rev. B* **41**, 7892 (1990).
- [69] H. J. Monkhorst and J. D. Pack, Special points for Brillouin-zone integrations, *Phys. Rev. B* **13**, 5188 (1976).
- [70] J. Ihm, D. H. Lee, J. D. Joannopoulos, and J. J. Xiong, Structural Phase Diagrams for the Surface of a Solid: A Total-Energy, Renormalization-Group Approach, *Phys. Rev. Lett.* **51**, 1872 (1983).
- [71] O. L. Alerhand and E. J. Mele, Surface reconstruction and vibrational excitations of Si(001), *Phys. Rev. B* **35**, 5533 (1987).
- [72] C. Xiao, X. Wang, X. Pi, S. A. Yang, Y. Feng, Y. Lu, and S. Zhang, Spontaneous symmetry lowering of Si(001) towards two-dimensional ferro/antiferroelectric behavior, *Phys. Rev. Mater.* **3**, 044410 (2019).
- [73] F. K. Men, W. E. Packard, and M. B. Webb, Si(100) Surface under an Externally Applied Stress, *Phys. Rev. Lett.* **61**, 2469 (1988).
- [74] A. García and J. E. Northrup, Stress relief from alternately buckled dimers in Si(100), *Phys. Rev. B* **48**, 17350 (1993).
- [75] G. Henkelman, B. P. Uberuaga, and H. Jónsson, A climbing image nudged elastic band method for finding saddle points and minimum energy paths, *J. Chem. Phys.* **113**, 9901 (2000), <https://doi.org/10.1063/1.1329672>.
- [76] H. Sato and K. Yagi, Surface stress on si(001)2*1 surfaces studied by tem, *Journal of Physics: Condensed Matter* **5**, 2095 (1993).
- [77] R. D. Meade and D. Vanderbilt, *The structure of surfaces* (Springer & Berlin, 1991).
- [78] J. Dąbrowski, E. Pehlke, and M. Scheffler, Calculation of the surface stress anisotropy for the buckled Si(001)(1 × 2) and p(2 × 2) surfaces, *Phys. Rev. B* **49**, 4790 (1994).
- [79] M. Webb, F. Men, B. Swartzentruber, R. Kariotis, and M. Lagally, Surface step configurations under strain: kinetics and step-step interactions, *Surface Science* **242**, 23 (1991).
- [80] H. A. Kramers and G. H. Wannier, Statistics of the Two-Dimensional Ferromagnet. Part I, *Phys. Rev.* **60**, 252 (1941).
- [81] H. Hobrecht and A. Hucht, Anisotropic scaling of the two-dimensional Ising model I: the torus, *SciPost Phys.* **7**, 26 (2019).

- [82] V. P. LaBella, D. W. Bullock, M. Anser, Z. Ding, C. Emery, L. Bellaiche, and P. M. Thibado, Microscopic View of a Two-Dimensional Lattice-Gas Ising System within the Grand Canonical Ensemble, *Phys. Rev. Lett.* **84**, 4152 (2000).
- [83] U. Scheithauer, G. Meyer, and M. Henzler, A new LEED instrument for quantitative spot profile analysis, *Surf. Sci.* **178**, 441 (1986).
- [84] M. Horn-von Hoegen, Growth of semiconductor layers studied by spot profile analysing low energy electron diffraction – Part I, *Z. Kristallogr. – Cryst. Mater.* **214**, 591 (1999).
- [85] A Debye temperature of $\Theta_D = (488 \pm 11_{\text{stat}})$ K is determined from the integrated intensity not shown here.
- [86] C. A. Tracy and B. M. McCoy, Examination of the phenomenological scaling functions for critical scattering, *Phys. Rev. B* **12**, 368 (1975).
- [87] A. Saxena, E. Gawlinski, and J. Gunton, Structural Phase Transitions on the Si(100) Surface, *Surf. Sci.* **160**, 618 (1985).
- [88] Y. Nakamura, H. Kawai, and M. Nakayama, Theory on STM images of Si(001) surface near defects, *Phys. Rev. B* **52**, 8231 (1995).
- [89] Y. Nakamura, H. Kawai, and M. Nakayama, Influence of defects on the order-disorder phase transition of a Si(001) surface, *Phys. Rev. B* **55**, 10549 (1997).
- [90] M. Okamoto, T. Yokoyama, T. Uda, and K. Takayanagi, Strain effects of missing dimer defects on dimer buckling of the Si(100) surface, *Phys. Rev. B* **62**, 12927 (2000).
- [91] M. Osanai, H. Yasunaga, and A. Natori, Dimer buckling dynamics in the vicinity of missing dimers on Si(100) surfaces, *Surf. Sci.* **493**, 319 (2001).
- [92] A. Natori, M. Osanai, J. Nakamura, and H. Yasunaga, Dynamics of $c(4 \times 2)$ phase-transition in Si(100) surfaces, *Appl. Surf. Sci.* **212–213**, 705 (2003), 11th International Conference on Solid Films and Surfaces.
- [93] H. Shigekawa, K. Miyake, M. Ishida, and K. Hata, Dynamics of Phasons, Phase Defects Formed on Dimer Rows, and Related Structural Changes of the Si(100) Surface at 80 K Studied by Scanning Tunneling Microscopy, *Jpn. J. Appl. Phys.* **36**, L294 (1997).
- [94] J. Wollschläger, Diffraction from surfaces with randomly distributed structural defects, *Surf. Sci.* **328**, 325 (1995).
- [95] T. W. B. Kibble, Topology of cosmic domains and strings, *J. Phys. A: Math. Gen.* **9**, 1387 (1976).

- [96] W. H. Żurek, Cosmological experiments in superfluid helium?, *Nature* **317**, 505 (1985).
- [97] C.-C. Fu, M. Weissmann, and A. Saúl, Molecular dynamics study of dimer flipping on perfect and defective Si(001) surfaces, *Surf. Sci.* **494**, 119 (2001).